

# “On the Land-Ocean Contrast of Tropical Convection and Microphysics Statistics Derived from TRMM Satellite Signals and Global Storm-Resolving Models”

Toshi Matsui<sup>1&2</sup>, Jiun-Dar Chern<sup>1&2</sup>, Wei-Kuo Tao<sup>1</sup>, Stephen Lang<sup>1&3</sup>,  
Masaki Satoh<sup>4</sup>, Tempei Hashino<sup>5</sup>, Takuji Kubota<sup>6</sup>

<sup>1</sup> Mesoscale Atmospheric Processes Laboratory, NASA/Goddard Space Flight Center, Greenbelt,  
MD 20771, USA

<sup>2</sup> Earth System Science Interdisciplinary Center, University of Maryland, College Park, MD  
20742, USA

<sup>3</sup> Science Systems and Applications Inc., Lanham, MD 20706, USA

<sup>4</sup> Atmosphere and Ocean Research Institute, The University of Tokyo, Japan

<sup>5</sup> Research Institute for Applied Mechanics, Kyushu University, Fukuoka, Japan

<sup>6</sup> Earth Observing Research Center, Japan Aerospace Exploration Agency, Japan

Submitted to Journal of Hydrometeorology

## Corresponding Author:

Toshi Matsui

Code 612, NASA Goddard Space Flight Center

Greenbelt, MD 20771

Tell: 301-614-5658

Email: [Toshihisa.Matsui-1@nasa.gov](mailto:Toshihisa.Matsui-1@nasa.gov)

**Abstract.** A 14-year climatology of Tropical Rainfall Measuring Mission (TRMM) collocated multi-sensor signal statistics reveal a distinct land-ocean contrast as well as geographical variability of precipitation type, intensity, and microphysics. Microphysics information inferred from the TRMM precipitation radar and Microwave Imager (TMI) show a large land-ocean contrast for the *deep* category, suggesting continental convective vigor. Over land, TRMM shows higher echo-top heights and larger maximum echoes, suggesting taller storms and more intense precipitation, as well as larger microwave scattering, suggesting the presence of more/larger frozen convective hydrometeors. This strong land-ocean contrast in deep convection is invariant over seasonal and multi-year time-scales. Consequently, relatively short-term simulations from two global storm-resolving models can be evaluated in terms of their land-ocean statistics using the TRMM Triple-sensor Three-step Evaluation via a satellite simulator. The models evaluated are the NASA Multi-scale Modeling Framework (MMF) and the Non-hydrostatic Icosahedral Cloud Atmospheric Model (NICAM). While both simulations can represent convective land-ocean contrasts in warm precipitation to some extent, near-surface conditions over land are relatively moisture in NICAM than MMF, which appears to be the key driver in the divergent warm precipitation results between the two models. Both the MMF and NICAM produced similar frequencies of large CAPE between land and ocean. The dry MMF boundary layer enhanced microwave scattering signals over land, but only NICAM had an enhanced deep convection frequency over land. Neither model could reproduce a realistic land-ocean contrast in in deep convective precipitation microphysics. A realistic contrast between land and ocean remains an issue in global storm-resolving modeling.

## 1. Introduction

Because of the smaller heat capacity of soil compared to water, the amplitudes of the diurnal cycle of surface total available turbulent (latent and sensible) heat flux and skin temperature tend to be greater over land than ocean. This likely amplifies lower-atmospheric heat energy in the afternoon, which often increases buoyant force, as measured by convective available potential energy (CAPE) (Pielke 2001). As a result, continental precipitation is most frequently observed from noon to late afternoon (Wallace 1975; Carbone et al. 2002; Matsui et al. 2010; Kikuchi and Wang 2008), and has been traditionally used to explain why continental convection is more vigorous than maritime (Williams and Stanfill 2002, hereafter referred to as WS02).

Lucas et al. (1994) investigated aircraft-measured vertical velocity within deep convection over ocean and land and found that the convective updraft cores of maritime systems are only a third or a half of the size of those of continental systems, although CAPE is similar between the two environments. WS02, Zipser et al. (2006), and Orville and Henderson (1986) similarly showed that continental convective precipitation systems tend to have more vigorous radar reflectivities and much higher lightning flash rates per storm as observed by the Tropical Rainfall Measuring Mission (TRMM) satellite. These convective clouds with frequent lightning suggest enhanced electric charge separation associated with mixed-phase cloud microphysics processes, accretion of supercooled cloud droplets onto ice crystals, and collision between the crystals and graupel particles (Williams et al. 2002; Williams et al. 2005; WS02; Takahashi 1978).

WS02 pointed out that the width of a thermal plume could be associated with the boundary layer height based upon the classic similarity theory of Morton et al. (1956). This simple parcel theory showed that a buoyant thermal parcel originating from point sources has a constant expansion ( $\sim 10^\circ$  expansion angle) toward the top of the boundary layer, leading to the following simple relationship between thermal width ( $W$ ) and boundary layer depth ( $D$ ):

$$W = 0.3525 D \quad (1)$$

From this equation, boundary layer depths of 1000m, 2000m, 3000m, and 4000m lead to thermal widths of 352m, 705m, 1057m, and 1410m, respectively. Although these estimates appear to be slightly higher than typical observations (Stull 1988), it does provide a basic physical explanation of how a deep continental boundary layer could generate wider updraft velocities in deep convection (Lucas et al. 1994).

WS02 also argued that land-ocean contrasts in cloud microphysics and dynamics should be associated with cloud-base heights. For example, maritime environments generally have a smaller surface sensible-to-latent heat flux ratio ( $\sim 0.1$ ), more surface relative humidity ( $\sim 80\%$ ), and a lower and warmer cloud base height ( $\sim 500$  m), all of which tends to enhance the warm rain process and create weaker updrafts and suppress supercooled water in deep convection. On the other hand, continental environments tends to have a much higher surface sensible-to-latent heat flux ratio ( $0.2\sim 1$ ), less surface relative humidity ( $20\sim 60\%$ ), and higher and colder cloud base heights ( $1000\sim 4000$ m), all of which tend to suppress warm rain processes and enhance supercooled water in the mixed-phase zone.

Larger concentrations of activated cloud condensation nuclei (CCN) associated with aerosols can increase the number concentration of cloud droplets while decreasing their sizes, which reduces the efficiency of warm rain processes. If further lifted above the  $0^\circ\text{C}$ -isotherm

level, the supercooled water will form ice crystals through various nucleation processes, enhancing latent heat release via the condensation of supercooled water and deposition of ice crystals in convective cores, all of which invigorate deep convection (Rosenfeld and Woodley 2000; Khain et al. 2008; Tao et al. 2007; Tao et al. 2012; and many others). Although not yet fully investigated, large non-hygroscopic aerosol particles can increase the concentration of ice forming nuclei (IFN), which likely enhances heterogeneous ice nucleation and latent heat release in deep convection (Tao and Matsui 2015). Both CCN and IFN are more largely concentrated over land than ocean (Demott et al. 2010), which could explain continental convective invigoration.

Robinson et al. (2011) recently showed examples of over-land convective invigoration through a set of idealized cloud-resolving model (CRM) simulations with various sized flat islands surrounded by ocean. Regardless of the different sets of microphysics schemes and large-scale forcing, scattering of CRM-generated microwave brightness temperature tends to become larger as the island size increases for different large-scale forcing and shows reasonable agreement with TRMM-observed microwave scattering (Williams et al. 2005; Zipser et al. 2006). They concluded that the dominant mechanism for convective invigoration over islands is mesoscale dynamics (pressure gradient) induced by the thermal contrast (the so called “thermal patch” effect) between the island and surrounding ocean and argued that boundary layer, surface humidity, and aerosol impacts are not significant for convective vigor over islands.

Further investigation requires more observational evidence over the spectrum of convection types, from shallow to deep convection, as well as large-scale high-resolution numerical experiments to better understand the physical mechanisms associated with land-ocean contrast. To this end, this study provides a climatological view of the contrast between oceanic

and continental convective precipitating clouds from long-term TRMM satellite multi-sensor statistics (Matsui et al. 2009). Unlike previous studies, this one extends the observational analysis from shallow to deep convective precipitating clouds in terms of spatial variability as well as tropical land-ocean composites (Section 2). This study is also the first attempt to investigate and understand how current global storm-resolving models can reproduce signals of land-ocean contrast in relation to satellite observations (Section 3). Finally, the capabilities, limitations and physical processes associated with the land-ocean contrast in convective systems are contrasted between the TRMM observations and the two global numerical cloud models (Section 4).

## **2. Observed TRMM climatology**

### **2.1 T3EF database**

This study utilizes the TRMM Triple-sensor Three-step Evaluation Framework [T3EF, (Matsui et al. 2009)] database, which is composed of co-located TRMM precipitation radar (PR) 13.8-GHz attenuation-corrected radar reflectivity from the TRMM 2A25 product (Iguchi et al. 2000), Visible Infrared Scanner (VIRS) 12- $\mu$ m infrared (IR) brightness temperature ( $Tb_{IR}$ ) from the TRMM 1B01 product, and TRMM Microwave Imager (TMI) 85.5-GHz dual-polarization microwave brightness temperature ( $Tb_{85}$ ) from the TRMM 1B11 product. The PR has a shorter wavelength than the TMI 85.5-GHz channels so that returned echo is sensitive to precipitating liquid and frozen particles. VIRS  $Tb_{IR}$  is sensitive to cloud droplets or ice crystal emission so

that it represents the cloud-top temperature of optically thick clouds. TMI  $Tb_{85}$  depression (i.e., scattering) is correlated with the amount of relatively small as well as large precipitation-sized ice particles, which provide additional information in convective system (Section 3c in Matsui et al. 2009). To construct the collocated signal database, convolution methods were applied upon the PR footprint.

This study extends the T3EF analysis over the entire Tropics over a 14-year period using the version 5 TRMM products in order to provide a T3EF perspective of the land-ocean contrast in cloud/precipitation processes. T3EF is compiled for each  $2.5^{\circ} \times 2^{\circ}$  grid box to show the spatial variability of precipitating cloud types and signal statistics as well as land/ocean-grouped statistics over the entire Tropics. A  $2.5^{\circ} \times 2^{\circ}$ -gridded global land-ocean mask is utilized to identify land and ocean grids. Overall statistics are limited to the TRMM orbital zone ( $37^{\circ}\text{S}$  to  $37^{\circ}\text{N}$ ), which is simply denoted as the Tropics in this study, although it contains sub-tropical zones.

## **2.2 Joint $Tb_{IR}$ - $H_{ET}$ precipitating cloud type diagrams**

The first part of T3EF categorizes precipitating clouds using collocated VIRS  $Tb_{IR}$  and PR  $H_{ET}$  (echo-top height) via joint histograms in order to analyze the precipitating cloud types, which was originally proposed by Masunaga et al. (2005). Radar  $H_{ET}$  is determined as having three successive layers (250m vertical bins) of significant PR reflectivity (i.e., a 20 dBZ threshold) and is calculated from ground level using a 5km-mesh digital elevation map. Thus,  $H_{ET}$  is above ground level. Also, the classification does not involve a bright-band analysis and is

independent from the TRMM 2A23 product (Awaka et al. 1998). This classification focuses on precipitating clouds by utilizing precipitation-height as well as cloud-top temperature information and has been widely used for characterizing tropical convective regimes (Masunaga et al. 2005), the phase of the Madden–Julian Oscillation (Lau and Wu 2010), and for evaluating cloud-resolving models (Stephen et al. 2004; Masunaga et al. 2008; Matsui et al. 2009).

If a PR  $H_{ET}$  is found, a precipitating cloud type is assigned to the column, depending on the VIRS  $Tb_{IR}$  and PR  $H_{ET}$  thresholds. Warm cloud tops ( $Tb_{IR} > 260^{\circ}\text{K}$ ) and shallow echo-top heights ( $H_{ET} < 4$  km) are assigned to the *shallow warm* (SW) category. A category with slightly colder cloud tops ( $Tb_{IR} > 245^{\circ}\text{K}$ ) and higher echo-top heights ( $4 \text{ km} < H_{ET} < 7 \text{ km}$ ) was previously defined as *congestus* (Masunaga et al. 2005; Matsui et al. 2009). The  $Tb_{IR}$  threshold of  $245^{\circ}\text{K}$  is based on that in Machado et al. (1998) for separating deep and non-deep clouds. However, this broad range of cloud-top temperatures also encompasses slightly deeper clouds than the traditional definition for *congestus* ( $\sim 260^{\circ}\text{K}$ , Johnson et al. 1999). Thus, in this study, this 2<sup>nd</sup> class is denoted as *mid-warm*. The *mid-cold* category represents either stratiform precipitation (Masunaga et al. 2005) or *congestus* overlapped by cirrus clouds (Stephen and Wood 2010) and has cold cloud-top temperatures ( $Tb_{IR} < 245^{\circ}\text{K}$ ) and the same storm tops as *mid-warm* ( $4 \text{ km} < H_{ET} < 7 \text{ km}$ ). The *deep* category includes deep stratiform areas and deep convection with cold cloud-top temperatures ( $Tb_{IR} < 260^{\circ}\text{K}$ ) and significantly higher echo-top heights ( $H_{ET} > 7 \text{ km}$ , see the schematics and discussion in Figure 1 in Matsui et al. 2009). Since this study extends into sub-tropical and mountainous regions, a new category, *shallow cold* ( $Tb_{IR} < 260^{\circ}\text{K}$  and  $H_{ET} < 4\text{km}$ ), is introduced. This new category represents shallow cold precipitation in sub-tropical regions or in the mountains as well as warm precipitating clouds overlapped by cirrus clouds.



The horizontal extent of cloud systems (i.e., cloud clusters) is also an important physical parameter for understanding tropical precipitation processes (Mapes and Houze 1993; Machado et al. 1998). Masunaga et al. (2005) found that horizontal precipitation and cloud correlation lengths, measured from TRMM  $H_{ET}$  and  $Tb_{IR}$ , consistently exceed 100 km in the *mid-cold* and *deep* categories, while they are limited to 8 – 18 km in the *shallow warm* and *mid-warm* categories. Although the database does not directly characterize their horizontal extents, the  $H_{ET}$ - $Tb_{IR}$ -based categories statistically suggest that the *mid-cold* and *deep* categories are more organized and clustered cloud-precipitation systems, while the *shallowwarm* and *mid-warm* categories are more isolated types.

Figure 1a shows joint  $Tb_{IR}$ - $H_{ET}$  diagrams over a 14-yr period for the entire tropics as well as their land-ocean difference. Based on the defined categories, the population of tropical precipitating cloud is 13.8% *shallow warm*, 17.9% *shallow cold*, 24.8% *mid-warm*, 28.4% *mid-cold*, and 14.7% *deep*. Land-ocean differences in the  $Tb_{IR}$ - $H_{ET}$  diagram reveal larger proportions of the *mid-warm* and *deep* categories over land but a much larger proportion of the *shallow warm* category over ocean. *Mid-cold* clouds are separated into relatively warmer (ocean) and colder (land)  $Tb_{IR}$  modes, respectively. These statistics essentially highlight the climatological land-ocean contrast in terms of cloud-precipitation types.

Figure 1b shows the spatial variations of the normalized frequencies for each category averaged over the 14-year period by constructing the  $Tb_{IR}$ - $H_{ET}$  diagram at each  $2.5^{\circ} \times 2^{\circ}$  grid. Thus, frequencies of five categories are summed up to 100% on each grid box. *Shallow warm* is the dominant precipitating cloud category over the southern portion of the Indian Ocean and the eastern portions of the Pacific and Atlantic Oceans. The total precipitation rate as well as the proportion of precipitating columns in these regions is very small, since most of these low clouds

have no drizzle signal or are undetectable by the PR instrument (Matsui et al. 2004). The majority of shallow precipitation occurs over ocean (Schumacher and Houze 2003), while shallow precipitation frequency over land is limited to coastal regions.

*Shallow cold* is more frequently found near the subtropical boundaries due to the presence of wintertime mid-latitude frontal systems and also over mountainous regions, such as the Rocky Mountains in North America, the western slopes of the Andes Mountains, and the Tibetan Plateau, where it is the most dominant precipitating cloud type (> 70%).

The *mid-warm* category mainly occurs over central North Africa over land and off the west coast of Namibia over ocean. *Mid-warm* is most likely observed in regions where hot, dry continental air from deserts engages with warm moist air masses, such as the semi-desert regions in Chad and Sudan, off the west coast of Namibia, the eastern part of the Arabian Peninsula and the center of Australia. Note that this class was previously defined as *congestus* (Masunaga et al. 2005; Matsui et al. 2009); however, the climatological map of relative frequencies differs from that estimated from CloudSat and TRMM data with different thresholds (Wall et al. 2013). Thus, the *mid-warm* class encompasses a broader range of precipitating clouds over tropical oceans than the *congestus* class (Masunaga et al. 2005; Stephen and Wood 2010).

The *mid-cold* category is most prevalent over the Pacific Warm Pool, the North and South Pacific Convergence Zones, the eastern portion of the Indian Ocean, and along the ITCZ over ocean. It also appears over central Africa, South America, India, and Southeast Asia over land. Because it has a large population with high rain intensities with larger clustering (Masunaga et al. 2005), the *mid-cold* category characterizes tropical precipitation variability. Therefore, the *mid-cold* frequency map closely resembles the precipitation climatology map (Wang et al. 2014). The highest (blue shade) *mid-cold* frequencies are observed off of the west

coasts of Burma, Sumatra, Borneo, and Central America. These regions have the largest annual precipitation rates from nocturnal stratiform precipitation (Mapes et al. 2003).

Finally, the *deep* category appears most over land, such as West Africa, India's Gangetic Basin, and Argentina's step regions where the most intense storms are typically observed (Zipser et al. 2006). These deep convective storms are commonly driven by strong CAPE, wind shear, and large-scale upward motion due to summertime monsoonal circulations and strong surface insolation. The highest frequencies (black shade) are found over Lake Chad in West Africa. In this region, up to 50% of precipitation pixels have storm heights greater than 7 km and cloud-top temperatures colder than 260 K.

### **2.3 Microphysical properties associated with categorized reflectivity CFADs**

The second step in T3EF is to construct contoured frequency with altitude diagrams (CFADs) (Yuter and Houze 1995) of PR reflectivity separately for the categories defined in the first step (section 2.2) in order to investigate precipitation microphysics (Matsui et al. 2009). Reflectivity CFADs were constructed for the entire tropics as well as their land-ocean difference by binning the reflectivities into 1-dBZ bins at each height increment (250m) (Figure 2a). Note that the sharp increase in reflectivity near the ground evident in all classes is most likely due to surface clutter.

Reflectivity intensities for the *shallow warm* and *shallow cold* categories are the weakest. Modal and maximum reflectivities are ~25 and 45 dBZ, respectively. Land-ocean differences in their CFADs show that both of these shallow categories have narrower reflectivity distributions over land than over ocean probably due to a lack of moisture as well as larger concentrations of

aerosols. The *mid-warm* and *mid-cold* categories have larger modal and maximum reflectivities than the *shallow warm* and *shallow cold* categories, and their land-ocean contrast shows that the land reflectivities tend to be more widely distributed, suggesting a larger variability of precipitation particle sizes (and rainfall intensity) over land.

*Shallow warm* and *mid-warm* show continuously increasing reflectivities toward the ground and suggests raindrop growth via coalescence processes, while the *mid-cold* category has a subtle bright band signal around 5 km, suggesting the presence of melting ice particles. Overlying solid particles above 7 km are invisible to the PR but not to infrared Tb and high-frequency microwave Tb (as shown in the next section and in the contrast between Figs. 3 and 4 in Matsui et al. 2009).

The most dramatic transitions in the reflectivity distributions are in the *deep* category where there are three distinct zones: the solid-phase (i.e., above 8 km, around -20°C (Hashino et al. 2013)) where the presence of solid precipitation particles statistically generates narrow reflectivity profiles, the mixed-phase (i.e., between 5 and 8 km) where the aggregation and melting of frozen particles dramatically increase reflectivity distributions, and the liquid-phase (i.e., below 5 km) where liquid raindrops dominate the radar backscattering signal. In this lowest, liquid-phase zone, profiles of near constant reflectivity distribution suggest raindrop size distributions are close to an equilibrium state through collision/coalescence growth and breakup processes (McFarquhar and List 1991) in a statistical sense.

Note that the CFADs for this class include data from various echo-top heights (i.e., 7-20 km). The reason for the relatively narrow echo distributions around 7 km is the dominant sampling of convection with echo-top heights of 7-10 km (e.g., Fig 1a). Alternatively, convection with echo-top heights greater than 10 km is statistically very small, which often

frustrates the interpretation of the CFADs. It should be understood that CFADs from a large sample volume would be slightly different from those from a single convective episode (e.g., Li et al. 2010).

Tao et al. (2015) decomposed a reflectivity CFAD from a cloud simulation with a bulk microphysics scheme (see their Fig. 8). Their study suggests that the majority of the mode reflectivities in the solid-phase zone are dominated by snow aggregates from the deep stratiform portion of their simulated MCS, while the infrequent occurrence of intense echoes is predominantly contributed by hail within the convective cores. In this way, strong reflectivities from a small area of convective cores and weak reflectivities from a large area of stratiform precipitation characterize the radar CFAD above the melting layer in what would be the *deep* category.

The land-ocean difference in CFADs also shows a clear contrast between maritime and continental environments. In the solid-phase zone ( $> 8$  km AGL, below  $-20^{\circ}\text{C}$ ), the land echo distributions trend to stronger values (red shading), while the ocean PR echo frequencies are more concentrated below  $\sim 24$  dBZ, which suggests a larger convective core fraction in the continental deep convective clouds. Below 8 km, continental echoes are more broadly distributed than oceanic as illustrated by the central blue mode shade surrounded by the red shading. This indicates that continental precipitation has a wider particle size spectrum (i.e., more smaller and more larger) than oceanic.

To better understand the large variability in the *deep* category, the spatial variability of echo-top height and maximum column echo are examined. PR CFADs are constructed for each  $2.0^{\circ} \times 2.5^{\circ}$  grid box over the Tropics; the 95% tile is then used to estimate the maximum PR echo-top height and column echo for the *deep* category. Figure 2b shows that *deep* convection tends

to have larger maximum column echoes (up to 50 dBZ) and taller echo-top heights (up to 15 km) over major continents than ocean. Continental convective invigoration is also apparent over the major islands in Southeast Asia, similar to the of Williams et al. (2004) and Robinson et al. (2011)..

## 2.4 Ice scattering from microwave Tbs

The third step of T3EF is to analyze the distributions of microwave Tb scattering. Scattering from high-frequency microwave channels is more directly associated with the path-integrated frozen hydrometeor amount than the surface precipitation rate, if there is enough ice aloft in the atmosphere. Otherwise, surface scattering signals dominate the scattering signals measured from the TMI. The 85-GHz TMI channels are fairly sensitive to smaller-sized frozen particles, which are often undetectable by the PR (Matsui et al., 2009). Because the TMI sampled mixed land-ocean areas over the Tropics, a polarization-corrected brightness temperature ( $PCTb_{85}$ ) is used to compensate for the inhomogeneity in surface emissivity (Spencer et al. 1989) via

$$PCTb_{85GHz} = Tb_{85V} + a (Tb_{85V} - Tb_{85H}),$$

where  $Tb_{85V}$  and  $Tb_{85H}$  are the  $Tb$  from the vertical and horizontal polarization channels at 85 GHz, respectively. Based on Matsui et al. (2009), a fixed value of  $a=0.8$  generally works well over the Tropics with the exception of some regions. This is close to the value (0.818) used in Spencer et al. (1989).

Figure 3a shows cumulative probability distributions of  $PCTb_{85}$  (the bin size is  $10^\circ\text{K}$ ) for all categories integrated over land and ocean. For each class, the Microwave Scattering Index (MSI) in this study is defined as

$$MSI = PCTb_{85\text{GHz}}|_{95\%} - PCTb_{85\text{GHz}}|_{5\%},$$

where  $PCTb_{85\text{GHz}}|_{5\%}$  and  $PCTb_{85\text{GHz}}|_{95\%}$  are the 5% tile and 95% tile of the cumulative distributions for each category in order to remove statistical outliers. Figure 3 shows cumulative distributions of  $PCTb_{85\text{GHz}}$  and MSI for the entire tropics as well as their land-ocean differences.

It is quite discernible that the probability distributions trend toward lower  $PCTb_{85}$  values as the cloud types progress from *shallow warm* to *mid-warm* to *shallow cold* to *mid-cold* to *deep* categories. MSI ranges from 29.82 to 100.2 K, which suggests that the amount of frozen particles increases substantially toward *deep* categories. Land-ocean differences show that the *deep* category is positive below 220 K and negative above and that the *mid-cold* category is positive below 240 K and negative above. This suggests that continental convection tends to have more solid ice processes than oceanic. Also note that there are substantial positive and negative variations in other categories, but these are most likely due to land-surface signals.

To assess spatial variability,  $PCTb_{85}$  probability distributions and MSI are computed for each  $2^\circ \times 2.5^\circ$  grid box to show the geographical distribution of ice scattering (Fig. 3b). MSI for the *shallow warm* category ranges from 0 to 30 K over ocean and from 10 to 40 K over land, which appears to be natural variability (gray shade) in the background microwave emission. Over the Tibetan Plateau, the MSI for the *shallow warm* category is anomalously large (up to 60 K) most likely due to presence of surface snow (Pulliainen and Hallikainen 2001). The polarization correction most likely failed to mask the surface signals due to the lack of column water vapor over the Plateau. Note that the scattering signals for *shallow warm* and *mid-warm*

are also affected by the slant angle of the TMI sensor viewing path, which often includes signals from neighboring cells with cold precipitation processes.

The MSI for *mid-cold* ranges from 10 to 70 K. A large MSI is associated with the regions where *mid-cold* is most frequently observed (Fig. 1b). The *deep* category has the largest variability of MSI, up to 110 K. Over ocean, the MSI for *deep* generally ranges up to 80 K, but in very limited regions such as the tropical warm pool, it can reach 90 K. The MSI for the *deep* category is clearly larger over land, including from central to southern Africa, India, South East Asia, northern Australia, and North and South America. Even over the islands in South East Asia, the MSI is typically ~10-20 K larger than the surrounding ocean, although the air mass should be maritime over land. This suggests that continental deep convection produces larger ice water paths than oceanic even within the same tropical air mass.

## **2.5 Mechanisms and robustness of land-ocean contrast**

Overall, Figs. 1-3 re-confirm that continental deep convection tends to have taller echo-top heights, larger maximum column reflectivities, and larger microwave scattering signatures than does maritime deep convection in agreement with previous studies (Williams et al. 2004; WS02; Zipser et al. 2006). Figure 4 summarizes the potential pathways for the invigoration of continental deep convection based on the aforementioned previous studies presented in Section 1. There are potentially four factors that could invigorate deep convection over land: i) amplified CAPE, ii) high surface sensible heat fluxes that lead to elevated cloud-base heights or the height of the lifting condensation level (HLCL), which then reduce warm cloud depth while also deepening the PBL depth and result in enhanced convective width and updraft velocity, iii) the



thermal patch effect wherein islands or land-cover patterns enhance mesoscale pressure gradients, wind convergence and consequently updraft velocity, and iv) higher aerosols concentrations which can reduce warm rain process via cloud nucleation. As evidenced from the TRMM climatology, all of these factors potentially can lead to the continental vigor of cloud and precipitation processes, namely the enhancement of deep convective processes and the concurrent suppression of warm rain processes (Fig. 1) along with an enhanced amount of supercooled water and more heavily rimed ice particles (Fig. 3), which result in deeper convection with more intense surface precipitation (Fig. 2).

Instead of using long-term climatology, this section briefly discusses the robustness of land-ocean contrast based on shorter time scales. Matsui et al. (2015) proposed the idea of convection-microphysics quasi-equilibrium (CMQE) states through a planetary view of tropical convection. They found that the characteristic spectrums of TRMM precipitation signals (radar echo and microwave brightness temperature spectra), precipitation rate, and microphysics states are nearly identical regardless of seasons and years as long as the sampling covered the entire Tropics, regardless of the day-to-day, seasonal, or inter-annual variability of tropical dynamics.

Figure 5a shows a monthly time series of the difference in composite PR CFADs for land minus ocean at mid levels (i.e., 3 km for *shallow warm* and *shallow cold*, 3.5 km for *mid-warm* and *mid-cold*, and 10 km for *deep*). There are some subtle but consistent land-ocean differences in the *shallow warm*, *shallow cold*, and *mid-warm* categories, close to the climatology difference in Fig. 2a. The *mid-cold* category, however, shows seasonal cycles in its land-ocean contrast. The most significant and consistent differences appear in the *deep* category, wherein continental deep clouds always show radar reflectivity invigoration within the solid-phase zone regardless of different months and years as long as the sampling is over the entire tropics.

Figure 5b shows a monthly time series of the difference in  $PCTb_{85}$  frequency between land and ocean in a similar manner to Fig. 5a. The  $PCTb_{85}$  distributions show clear land-ocean differences for all categories. Consistent positive signals for the *shallow warm* and *shallow cold* signals are due to land-surface signals, which are mostly likely not associated with differences in the microphysical characteristics between land and ocean environments. *Mid-warm* signals are also inconsistent throughout the time-series so that there is no time-consistent land-ocean  $PCTb_{85}$  due to the lack of appreciable amounts of ice in this class. At times, *mid-warm* over-ocean has  $PCTb_{85}$  probability densities that are more narrowly distributed, but the results are relatively sporadic. The *mid-cold* category has more distinct land-ocean differences in  $PCTb_{85}$ , though the PR CFAD results are nearly identical between land and ocean. This could be due to either a difference between land and ocean in the tiny precipitating ice to which the  $PCTb_{85}$  is sensitive, and/or the TMI slant beam path is including *deep* category signals. The *deep* category has the most distinct and consistent differences with the over-land microwave signal always having stronger scattering due to the larger amount of precipitating ice in the mixed-phase zone.

These results confirm that the continental invigoration of deep convection is always present regardless of the month and year. As suggested by the CMQE hypothesis (Matsui et al. 2015), the land-ocean contrast could be evident at even finer temporal resolutions (e.g., daily) provided there is a sufficient number of convective samples. Alternatively, land-ocean contrast can also be investigated at short time periods if enough sampling can be obtained from high-resolution global simulations.

### 3. Land-ocean contrast in global storm-resolving models

### 3.1 Global storm-resolving models

Using the new observational benchmark for convective land-ocean contrast through T3EF, the main objective of this section is to evaluate for the first time the land-ocean contrast simulated by global high-resolution model simulations over a relatively shorttime period. The impact of aerosols, however, is not investigated, as it is not predicted in the models. The simulations that will be tested are from the NASA Multi-scale Modeling Framework (MMF) and the Non-hydrostatic Icosahedral Cloud Atmospheric Model (NICAM). Both simulations are designed to resolve organized convection with horizontal grid spacings of 4 and 3.5 km, respectively.

The NASA MMF is based on the Goddard Earth Observing System V4 (GEOS4) with the convection and microphysics parameterizations replaced by explicit 2D CRM simulations using the Goddard Cumulus Ensemble (GCE) model (Tao et al. 2009; Tao et al. 2014). The MMF uses the Community Land Model (CLM) (Bonan et al. 2002) to predict the land surface turbulent heat flux and skin temperature in each GEOS4 grid. The MMF was initialized with European Center for Medium range Weather Forecasting (ECMWF) interim re-analysis (ERA-interim) (Dee et al. 2011) and integrated over the entire month of June 2008.

NICAM was developed to study the capabilities of fully 3D global CRMs (Tomita and Satoh 2004; Satoh et al. 2008, 2014). The NICAM experiment in this study was designed to study tropical cyclone (TC) Fengshen from its genesis stage to its mature stage (Hashino et al. 2013). The winds, temperature, relative humidity, and geopotential heights in the NICAM simulation were initialized with the 0.5° ECMWF Year of Tropical Convection (YOTC) analysis at 00:00 UTC 15 June 2008 (Moncrieff et al. 2012) and integrated for one week only. The

surface variables such as sea surface temperature (SST), sea ice cover, and soil moisture are initialized with 1° National Centers for Environmental Prediction (NCEP) reanalysis.

The MMF and NICAM use the Goddard single-moment 4ICE (Lang et al. 2014) and the NICAM Single-moment Water 6 (NSW6) (Tomita 2008) cloud microphysics schemes, respectively. Both 4ICE and NSW6 are based on the Lin (Lin et al. 1983) and Rutledge and Hobbs (Rutledge and Hobbs 1983) schemes, but NSW6 omits the wet growth of hail in order to reduce computation cost. The 4ICE scheme has been developed based on a series of improvements using observations (Tao et al. 2003; Lang et al. 2007; Lang et al. 2011). The most recent updates (Lang et al., 2014; Tao et al. 2016) include newer diagnostic snow and graupel size distributions and a new frozen drops-hail category for severe thunderstorms as well as other improvements. Table 1 summarizes the MMF and NICAM model set up and physics options.

NICAM has a realistic land mask, terrain, and land-cover specification, permitting “thermal patch” effects due to sea breezes and/or land-cover heterogeneity, while the NASA MMF only generates homogeneous surface energy and turbulent fluxes driven by the GEOS4 CLM. Thus, both the MMF and NICAM could be used to examine the impact of variations in the HLCL and large-scale CAPE, while only NICAM is capable of producing a realistic “thermal patch” effect (Fig. 4).

### **3.2 Satellite simulators**

Model-simulated geophysical parameters (including cloud and precipitation microphysics information) from the MMF and the NICAM simulations are converted into TRMM signals

through the Goddard Satellite Data Simulator Unit (G-SDSU, Matsui et al. 2013, 2014) and the Joint Simulator for Satellite Sensors (Hashino et al. 2013). Both multi-instrumental simulators employ identical microwave simulators (Kummerow 1993), radar simulators (Masunaga and Kummerow 2005), and IR simulators (Nakajima and Tanaka 1986). Details on the computation methods are described in previous studies (Matsui et al. 2009, 2014).

Briefly, the effective dielectric function is calculated from the Maxwell-Garnett assumption, and single scattering properties are calculated from the Mie assumption for both microwave and radar simulators. The microwave simulator can account for slant-path beams, mimicking the 3D slant-path observations in conical-scanning microwave radiometers, such as the TMI. These forward models are consistent with the physics assumptions (including the particle size distributions, phase, and effective densities) within the microphysics schemes used in the MMF and NICAM. VIRS  $Tb_{IR}$ , PR  $H_{ET}$ , PR CFAD, and TMI  $PCTb_{85}$  are simulated in each of the MMF columns and the NICAM output and sampled in an identical manner to the TRMM observations.

### 3.3 Simulated T3EF diagrams from the MMF and NICAM

Figure 6a shows  $Tb_{IR}$  -  $H_{ET}$  diagrams derived from TRMM observations, the MMF simulation, and the NICAM simulation for the entire Tropics over both land and ocean for June 2008. Figure 6b shows the corresponding land-ocean differences. The June TRMM  $Tb_{IR}$  -  $H_{ET}$  diagram for the combined land-ocean average has a very similar pattern to the climatology (Figure 1a). Also similar to the climatology, monthly land-ocean differences in the  $Tb_{IR}$  -  $H_{ET}$

485 diagram reveal larger proportions of the *mid-warm* and *deep* categories over land but a much  
486 larger proportion of the *shallow warm* category over ocean.

487 The structure of the MMF  $Tb_{IR}$  - $H_{ET}$  diagrams is somewhat closer to the TRMM  
488 observations. However, its joint PDF is skewed more towards the *shallow warm* and *shallow*  
489 *cold* categories and misses a large portion of *mid-warm*. The *shallow cold* category is nearly  
490 twice as much as for the TRMM observations. The land-ocean contrast for the MMF appears to  
491 be quite good in agreement in terms of its larger proportion of maritime *shallow warm* (blue  
492 shading in zone 1) and continental *mid-warm* (red shading in zone 2). The MMF, however,  
493 produces a higher portion of vigorous convection over ocean as depicted by the blue shading in  
494 the *deep* category, unlike the TRMM observations. Also, its maritime *mid-cold* peak is skewed  
495 towards *shallow cold* (zone 5, near echo-top heights of ~4 km). As a result, *mid-cold* appears at  
496 a higher frequency over land.

497 The structures of the NICAM  $Tb_{IR}$  - $H_{ET}$  diagrams appear to be somewhat different from  
498 the TRMM observations as well as from those of the MMF. The *shallow warm* category is over  
499 twice the TRMM-observed frequency, while the *deep* distribution extends to much higher  $H_{ET}$  (>  
500 10 km) than do the TRMM observations or the MMF simulations, which occur predominantly  
501 under 10 km. Similar to the MMF results, there are no distinct peaks in the *mid-warm* and *mid-*  
502 *cold* zones. NICAM produces the correct land-ocean contrast in the form of higher frequencies  
503 over land for the *deep* category and higher frequencies over ocean for the *shallow warm*, though  
504 they are too strong and too weak, respectively. The continental *mid-warm* peak is also quite  
505 evident, but the echo-top heights are too shallow relative to the TRMM observations and as a  
506 result appear as *shallow warm*.

Since the NICAM integration time is much shorter than the TRMM observations and the MMF simulation, the spatial distributions of these precipitating cloud types are not discussed in the main article. However, the reader is encouraged to view the detailed spatial maps and discussion in the supplemental material (SUPPLEMENTAL A).

Figure 7a shows PR CFADs for the *deep* category from the TRMM observations, the MMF simulation, and the NICAM simulation for the entire Tropics over both land and ocean for the same time period. Both the MMF and NICAM reproduce reasonable PR CFAD structures. At upper levels ( $> 8$  km AGL), the MMF echoes are more narrowly distributed due to the specified snow aggregate and graupel size distributions and effective densities (Lang et al. 2014). In contrast, the NICAM CFAD is more broadly distributed and tends to overestimate PR echoes at all levels.

Figure 7b shows the corresponding land-ocean contrast in PR CFADs for the *deep* category. The monthly TRMM observations show a clear land-ocean contrast in the PR echo distributions, nearly identical to the climatology (Fig. 2). The MMF simulation has a mixture of results. Above 10 km, continental echoes are shifted to larger values as observed; however, below 10 km, the oceanic distributions are broader (i.e., the red shading is surrounded by blue), which is opposite to the observations. It is probably due to the invigoration of oceanic deep convection in the MMF simulation (Fig. 6b). The NICAM simulation shows signs of continental invigoration above 5 km similar to the observations, but the signal is weaker than the TRMM observations and less coherent throughout the vertical range. In the warm-precipitation zone below 5 km, as with the MMF, the results are counter to TRMM with broader oceanic distributions. The results are discussed more in the next section.

Figure 8a shows cumulative frequencies of  $PCTb_{85}$  (with a bin size of  $10^\circ\text{K}$ ) for the *deep* category from the TRMM observations, the MMF simulation, and the NICAM simulation. The MMF-simulated  $PCTb_{85}$  is distributed over much colder temperatures than the observations. NICAM also overestimates the  $PCTb_{85}$  depression; however, it performs better than the MMF. This indicates that the MMF and NICAM overproduce solid precipitation particles in deep convection environments, which has been a common problem in CRMs due to unresolved microphysics and dynamics (e.g., Varble et al. 2014).

The TRMM land-ocean difference (Fig. 8b) in  $PCTb_{85}$  is positive below 240 K and negative above and suggests that continental convection tends to have more solid ice processes than oceanic. The MMF land-ocean difference in  $PCTb_{85}$  is more exaggerated; positive frequency differences (i.e., a higher land frequency) reach nearly 6.5% from  $\sim 170$ -180 K. There are small negative deviations above  $\sim 220$  K, but they are rather weak. The MMF therefore does not reproduce continental invigoration in its PR signals, but it does in its TMI signals. The positive  $PCTb_{85}$  frequency deviations below  $\sim 220$  K in NICAM are comparable to the TRMM observations but the negative deviations (i.e., higher oceanic frequencies) are lacking.

To verify the background model dynamics, the updraft velocities and thermodynamic states from the MMF and NICAM simulations are investigated. Figure 9 shows CFADs of vertical velocity over the entire tropics as well as their land-ocean difference. The MMF CFAD exhibits two subtle downdraft modes that peak around 2-4 km and 12-14 km of altitude, while peak updraft velocities appear near 10 km of altitude. The MMF CFAD shows that 99.9% of all vertical velocities (color shades) are less than  $5 \text{ m s}^{-1}$ . At a frequency of  $10^{-5} \%$  (outer edge of darkest gray shade), updrafts reach up to  $20 \text{ m s}^{-1}$ . The land-ocean difference shows a wider spread of updraft velocities (i.e., a higher portion of strong updrafts and strong downdrafts, red



shading) over land, especially from 2-10 km of altitude. This might explain the MMF's land dominance in the 2<sup>nd</sup> and 3<sup>rd</sup> categories of the  $Tb_{IR}$ - $H_{ET}$  composites (Fig. 6b).

The NICAM CFAD exhibit two distinct modes of stronger downdrafts near ~14 and from 2-4 km. Peak updraft velocities occur slightly higher in NICAM (~12 km) than in the MMF (~10 km) and are more intense at the  $10^{-5}$  % frequency, up to  $27 \text{ m s}^{-1}$ . The difference between land and ocean shows a wider distribution of updraft velocities over land, especially from 12–18 km of altitude. This explains the continental vigor in deep convection in the NICAM simulation. It requires more case-by-case comparison with the observed quantities in future study (e.g., Heymsfield et al. 2010).

Figure 10a shows the environmental thermodynamic states over land and over ocean, namely the convective available potential energy (CAPE) and the height of the lifting condensation level (HLCL) in clear-sky conditions (due to the data availability) from Aqua Atmospheric Infrared Sounder (AIRS) Level 2 data and all-sky conditions from the MMF and NICAM simulations. For larger CAPE ( $> 2000 \text{ J Kg}^{-1}$ ), the MMF's frequency curves over land and ocean are nearly identical to each other; the same is true for NICAM. In comparison to the observations, the MMF's oceanic CAPE curve is closer to the AIRS pattern, while over land the NICAM's CAPE distribution is much closer to the AIRS pattern than the MMF's. However, the AIRS retrievals are severely limited over land due to cloud contamination for the larger CAPE conditions, and AIRS sampling took place during the local early afternoon. Furthermore, it is technically difficult to derive CAPE values only prior to the onset of deep convection from both the AIRS observations and the MMF/NICAM simulations. Regardless of the uncertainties, it is confirmed that CAPE between land and ocean over tropical regions show relatively small

contrast in each of the MMF and NICAM simulations, consistent with previous observational studies (WO02; Williams and Renno 1993; Lucas et al. 1996).

HLCL clearly shows a strong land-ocean contrast, especially for AIRS and the MMF. Maritime conditions tend to have a significantly shallower HLCL due to the dominance of surface turbulent latent heat fluxes, while HLCL values are much deeper over land due to the dominance of turbulent sensible heat fluxes. The MMF has a higher frequency of very deep HLCLs over land than does NICAM. This suggests that NICAM is characterized with moister boundary layer conditions than the MMF over land, which results in NICAM having shallower HLCL values. This then leads to the NICAM biases associated with the lack of separation between *shallow warm* and *mid-warm* clouds (Fig. 6b). On the other hand, drier boundary layer conditions in the MMF likely suppressed warm rain process but increased production of ice crystals, resulting in the larger ice scattering signals over land (Figs. 4 & 8) despite having similar CAPE over land and ocean.

Figure 10b shows the lowest-layer relative humidity (RH) and surface evaporative fraction (EF: latent heat flux over total latent and sensible heat flux) from the MMF and the NICAM simulations. Over ocean, the MMF and NICAM show very similar distributions and largely skewed toward larger RH and EF values. Over land, the MMF has broader distributions of RH and EF with NICAM having narrower, moister distributions. This suggests that NICAM tends to have larger surface latent heat fluxes that induce higher boundary layer humidity and lower HLCLs than in the MMF. This subsequently lowers the cloud altitude for the continental *mid-warm* type into the *shallow warm* class, resulting in an overestimation of the *shallow warm* class in the NICAM simulation.

### 3.4 Summary and discussion

An initial attempt at evaluating the land-ocean contrast in convection and microphysics processes from two global storm-resolving models has been conducted. To some extent, the MMF simulations reproduced the observed pattern of land-ocean contrast for the *shallow warm* and *mid-warm* types (Fig. 6b). This is most likely because the MMF reproduced a realistic land-ocean contrast in HLCL (Fig. 10a). These results suggest the importance of the pathway associated with high sensible heat fluxes over land in Fig. 4 (WS02). Drier surface fluxes also elevate boundary layer heights, which would favor the creation of more *mid-warm* clouds as shown by the  $Tb_{IR}$ - $H_{ET}$  diagrams (Fig. 6b). The NICAM simulation tends to have much wetter surface soil conditions, which induces a larger evaporative fraction and higher relative humidity. As a result, it lowers cloud altitudes from *mid-warm* to *shallow warm* types, resulting in its continental *mid-warm* (i.e., *congestus*) mode conforming more to the *shallow warm* category (Fig. 6b). As a result, the NICAM simulation overestimates the *shallow warm* class over the tropics (Fig. 6a). Supplemental material also shows extensive and excessive distributions of shallow warm clouds over desert region (Supplemental A).

Although the magnitude and extent were not quantitatively consistent with the observations (Fig. 8a), both the MMF and NICAM simulations generated more  $PCTb_{85}$  ice-scattering in continental convection (Fig 8b), suggesting they produced more solid ice particles in their deep continental convective mode despite the large CAPE distributions being very similar between land and ocean (Fig. 10a). However, neither the MMF nor NICAM generated a realistic land-ocean contrast in their radar signals as depicted by PR CFADs (Fig. 7b). Structural

differences in the simulated CFADs between land and ocean are less coherent in the vertical direction, unlike those from the TRMM PR, which show clear, coherent patterns through solid, mixed, and liquid-phase precipitation.

The results are also interesting due to the fact that the MMF modeling setup does not account for the “thermal patch” effect. Robinson et al. (2011) concluded that mesoscale wave dynamics due to the “thermal patch” effect is the primary mechanism for continental convective vigor over islands. At least, despite homogeneous surface fluxes in the MMF and nearly identical CAPE distributions between land and ocean, stronger scattering signals were simulated in continental deep convection primarily due to the drier surface conditions (i.e., higher HLCL) (WS02). Of course, these results do not reject the finding in Robinson et al. (2011), because the MMF simulation does not reproduce more frequent deep convection (as measured by  $Tb_{IR}$  and  $H_{ET}$ ) over land, while the NICAM simulation does. From these simulations, it can be concluded that i) drier surface fluxes contribute to the generation of *mid-warm* types of clouds and glaciation of deep convection and ii) the thermal patch effect is important for generating more frequent deep convection and taller storm-top heights in continental deep convection.

Quantifying the surface sensible heat flux impact and “thermal-patch” impact requires that the physics, grid configurations, and initial and boundary conditions between the MMF and NICAM be more similar. The overall results indicate that even these advanced global storm-resolving modeling systems have room to improve their microphysics and dynamics in order to replicate the nature of the observed land-ocean contrast in convection, as suggested by previous evaluation studies (Masunaga et al. 2008; Inoue et al. 2010; Satoh et al. 2010; Kodama et al. 2012; Roh and Satoh 2014).

There are some pathways for improving the weaknesses in the simulations associated with the surface conditions, resolution, and the sophistication of the microphysics. The spin-up of soil moisture for initial conditions in NICAM and MMF could potentially be improved for more realistic CAPE, but would require a more careful setup for future experiments (Mohr 2013). Although traditionally known as “cloud-resolving models”, a typical grid spacing of 1 to 4 km and ~60 vertical levels will only resolve cloud systems greater than ~5 to 40 km (Pielke 2013). Khairoutdinov et al. (2009) showed a clear improvement in simulating shallow/congestus populations when the horizontal grid spacing was reduced to 200 m and vertical levels increased to 256. It is also important to couple with realistic aerosol simulations to obtain CCN and IFN in order to investigate whether aerosols really help to characterize a realistic convective land-ocean contrast in future (Saleeby and van den Heever 2013).

It must be emphasized that analyzing global storm-resolving models provides a more comprehensive pathway for more universal understanding, including the land-ocean contrast.. However, this approach requires a lot more computing resources. But, such improvement is needed to fulfill the desire to simulate a more realistic land-ocean contrast (Lucan et al. 1994; Williams et al. 2002; Williams et al. 2005; WS02, Liu and Zipser 2005).

660 **Acknowledgements.** This study has been funded by the NASA Modeling, Analysis and  
661 Prediction (MAP) program (Project Manager: D. Considine at NASA HQ). Drs T. Matsui, J.  
662 Chern, W.-K. Tao, and Mr. S. Lang are also funded by the NASA Precipitation Measurement  
663 Missions (PMM) program (Project Manager: R. Kakar at NASA HQ). We also thank the NASA  
664 Advanced Supercomputing (NAS) Division (Project Manager: T. Lee at NASA HQ) for  
665 providing the computational resources. The lead author (T. Matsui) would like to give special  
666 thanks to Dr. E. Zipser at the U. of Utah for his useful discussions.

**References:**

- Awaka, J., T. Iguchi, and K. Okamoto, 1998: Early results on rain type classification by the Tropical Rainfall Measuring Mission (TRMM) precipitation radar. Proc. 8th URSI Commission F Open Symp., Aveiro, Portugal, 143-146.
- Bonan, B. G., K. W. Oleson, M. Vertenstein, S. Levis, X. Zeng, Y. Dai, R. E. Dickinson, and Z.-L. Yang, 2002: The Land Surface Climatology of the Community Land Model Coupled to the NCAR Community Climate Model. *J. Climate*, **15**, 3123–3149.
- Carbone, R. E., J. D. Tuttle, D. A. Ahijevych, and S. B. Trier (2002), Inferences of predictability associated with warm season precipitation episodes, *J. Atmos. Sci.*, **59**, 2033–2056, doi:10.1175/1520-0469(2002) 059<2033:IOPAWW>2.0.CO;2.
- Dalu, G., R. Pielke, M. Baldi, and X. Zeng, 1996: Heat and momentum fluxes induced by thermal inhomogeneities with and without large-scale flow. *J. Atmos. Sci.*, **53**, 3286-3302.
- Demott, P. J., A. J. Prenni, X. Liu, S. M. Kreidenweis, M. D. Petters, C. H. Twohy, M. Richardson, T. Eidhammer, and D. Rogers, 2010: Predicting global atmospheric ice nuclei distributions and their impacts on climate. *Proceedings of the National Academy of Sciences*, **107**, 11217-11222.
- Dee, D. P., et al. (2011), The ERA-Interim reanalysis: configuration and performance of the data assimilation system. *Q.J.R. Meteorol. Soc.*, **137**: 553–597. doi: 10.1002/qj.828
- Hashino, T., M. Satoh, Y. Hagihara, T. Kubota, T. Matsui, T. Nasuno, and H. Okamoto, 2013: Evaluating cloud microphysics from NICAM against CloudSat and CALIPSO. *Journal of Geophysical Research: Atmospheres*, **118**, 1-20.

688 Heymsfield, G. M., L. Tian, A. J. Heymsfield, L. Li, and S. Guimond, 2010: Characteristics of  
 689 Deep Tropical and Subtropical Convection from Nadir-Viewing High-Altitude Airborne  
 690 Doppler Radar. *J. Atmos. Sci.*, **67**, 285–308. doi: <http://dx.doi.org/10.1175/2009JAS3132.1>  
 691 Iguchi, T., T. Kozu, R. Meneghini, J. Awaka, and K. Okamoto, 2000: Rain-Profiling Algorithm  
 692 for the TRMM Precipitation Radar. *J. Appl. Meteor.*, **39**, 2038–2052. doi:  
 693 [http://dx.doi.org/10.1175/1520-0450\(2001\)040<2038:RPAFTT>2.0.CO;2](http://dx.doi.org/10.1175/1520-0450(2001)040<2038:RPAFTT>2.0.CO;2)  
 694 Inoue, T., Satoh, M., Hagihara, Y., Miura, H., and Schmetz, J., 2010: Comparison of high-level  
 695 clouds represented in a global cloud system resolving model with CALIPSO/CloudSat and  
 696 geostationary satellite observations. *J. Geophys. Res.*, **115**, D00H22,  
 697 doi:10.1029/2009JD012371.  
 698 Johnson, R. H., T. M. Rickenbach, S. A. Rutledge, P. E. Ciesielski, and W. H. Schubert, 1999:  
 699 Trimodal characteristics of tropical convection. *J. Climate*, **12**, 2397–2418.  
 700 Khain, A. P., N. Benmoshe, and A. Pokrovsky, 2008: Factors determining the impact of aerosols  
 701 on surface precipitation from clouds: An attempt at classification. *J. Atmos. Sci.*, **65**, 1721-  
 702 1748.  
 703 Khairoutdinov M. F., S. K. Krueger, C.-H. Moeng, P. A. Bogenschutz and D. A. Randall, 2009:  
 704 Large-eddy simulation of maritime deep tropical convection. *Journal of Advances in*  
 705 *Modelling Earth Systems* Vol. 1, Art. #15, 13 pp., doi:10.3894/JAMES.2009.1.15  
 706 Kikuchi, K., and B. Wang, 2008: Diurnal precipitation regimes in the global tropics, *J. Clim.*, **21**,  
 707 2680–2696, doi:10.1175/2007JCLI2051.1.  
 708 Kodama, C., Noda, A.T., Satoh, M., 2012: An Assessment of the Cloud Signals Simulated by  
 709 NICAM using ISCCP, CALIPSO, and CloudSat Satellite Simulators. *J. Geophys. Res.*,  
 710 **117**,D12210, doi:10.1029/2011JD017317.



711 Kondo, J., 1993: A new bucket model for predicting water content in the surface model. *J. Japan*  
712 *Soc. Hydrol. and Water Res.* **6**, 344-349.

713 Kummerow, C., 1993: On the accuracy of the eddington approximation for radiative transfer in  
714 the microwave frequencies. *J. Geophys. Res.*, **98**, 2757-2765.

715 Lang, S., W.-K. Tao, R. Cifelli, W. Olson, J. Halverson, S. Rutledge, and J. Simpson, 2007:  
716 Improving simulations of convective systems from trmm lba: Easterly and westerly  
717 regimes. *J. Atmos. Sci.*, **64**, 1141-1164.

718 Lang, S. E., Wei-Kuo Tao, Jiun-Dar Chern, Di Wu, and Xiaowen Li, 2014: Benefits of a Fourth  
719 Ice Class in the Simulated Radar Reflectivities of Convective Systems Using a Bulk  
720 Microphysics Scheme. *J. Atmos. Sci.*, **71**, 3583–3612.

721 Lang, S. E., W.-K. Tao, X. Zeng, and Y. Li, 2011: Reducing the biases in simulated radar  
722 reflectivities from a bulk microphysics scheme: Tropical convective systems. *Journal of*  
723 *the Atmospheric Sciences*, **68**, 2306-2320.

724 Lau, K-M., and H-T. Wu, 2010: Characteristics of Precipitation, Cloud, and Latent Heating  
725 Associated with the Madden–Julian Oscillation. *J. Climate*, **23**, 504–518. doi:  
726 <http://dx.doi.org/10.1175/2009JCLI2920.1>

727 Li, X., W.-K. Tao, T. Matsui, C. Liu, and H. Masunaga (2010), Improving a spectral bin  
728 microphysical scheme using long-term TRMM satellite observations. *Quarterly Journal of*  
729 *Royal Metrological Society*, 136(647), 382-399.

730 Lin, Y.-L., R. D. Farley, and H. D. Orville, 1983: Bulk parameterization of the snow field in a  
731 cloud model. *J. Clim. Appl. Meteor.*, **22**, 1066-1092.

732 Liu, C., and E. J. Zipser, 2005: Global distribution of convection penetrating the tropical  
733 tropopause. *Journal of Geophysical Research: Atmospheres (1984–2012)*, **110**,

734 Lucas, C., E. J. Zipser, and M. A. Lemone, 1994: Vertical velocity in oceanic convection off  
 735 tropical Australia. *Journal of the atmospheric sciences*, **51**, 3183-3193  
 736 Machado, L. A. T., W. B. Rossow, R. L. Guedes, and A. W. Walker, 1998: Life cycle variations  
 737 of mesoscale convective systems over the Americas. *Mon. Wea. Rev.*, **126**, 1630–1654.  
 738 Mapes, B. E., T. T. Warner, M. Xu, and A. J. Negri, 2003: Diurnal patterns of rainfall in  
 739 northwestern south america. Part I: Observations and context. *Monthly Weather Review*,  
 740 **131**, 799-812.  
 741 Mapes, B.E., and R. A. Houze Jr., 1993: Cloud Clusters and Superclusters over the Oceanic  
 742 Warm Pool. *Mon. Wea. Rev.*, **121**, 1398–1416. doi: [http://dx.doi.org/10.1175/1520-](http://dx.doi.org/10.1175/1520-0493(1993)121<1398:CCASOT>2.0.CO;2)  
 743 [0493\(1993\)121<1398:CCASOT>2.0.CO;2](http://dx.doi.org/10.1175/1520-0493(1993)121<1398:CCASOT>2.0.CO;2)  
 744 Masunaga, H., T. S. L’Ecuyer, and C. D. Kummerow (2005), Variability in the characteristics of  
 745 precipitation systems in the tropical Pacific. Part I: Spatial structure, *J. Clim.*, **18**, 823– 840.  
 746 Masunaga, H., and C. Kummerow, 2005: Combined radar and radiometer analysis of  
 747 precipitation profiles for a parametric retrieval algorithm. *J. Atmos. Ocean. Tech.*, **22**, 909-  
 748 929.  
 749 Masunaga, H., Satoh, M., Miura, H., 2008: A Joint Satellite and Global CRM Analysis of an  
 750 MJO event: Model Diagnosis. *J. Geophys. Res.*, doi:10.1029/2008JD009986, 113, D17210.  
 751 Matsui, T., H. Masunaga, R. A. Pielke Sr., and W.-K. Tao, 2004: Impact of aerosols and  
 752 atmospheric thermodynamics on cloud properties within the climate system. *Geophysical*  
 753 *Research Letters*. 31(6), L06109, 10.1029/2003GL019287.  
 754 Matsui, T., X. Zeng, W.-K. Tao, H. Masunaga, W. S. Olson, and S. Lang, 2009: Evaluation of  
 755 long-term cloud-resolving model simulations using satellite radiance observations and

756 multifrequency satellite simulators. *Journal of Atmospheric and Oceanic Technology*, **26**,  
757 1261-1274.

758 Matsui, T., D. Mocko, M.-I. Lee, W.-K. Tao, M. J. Suarez, and R.A. Pielke Sr. 2010: Ten-year  
759 climatology of summertime diurnal rainfall rate over the conterminous U.S., *Geophysical*  
760 *Research Letters*, **37**, L13807, doi:10.1029/2010GL044139.

761 Matsui, T., J. Santanello, J. J. Shi, W.-K. Tao, D. Wu, C. Peters-Lidard, E. Kemp, M. Chin, D.  
762 Starr, M. Sekiguchi, and F. Aires, (2014): Introducing multisensor satellite radiance-based  
763 evaluation for regional Earth System modeling, *Journal of Geophysical Research*, **119**,  
764 8450–8475, doi:10.1002/2013JD021424.

765 Matsui, T., T. Iguchi, X. Li, M. Han, W.-K. Tao, W. Petersen, T. L'Ecuyer, R. Meneghini, W.  
766 Olson, and C. D. Kummerow, 2013: GPM satellite simulator over ground validation sites.  
767 *Bulletin of the American Meteorological Society*, **94**, 1653-1660.

768 Matsui, T., W.-K. Tao, S. J. Munchack, G. Huffman, and M. Grecu (2015), Satellite View of  
769 Quasi-Equilibrium States in Tropical Convection and Precipitation Microphysics,  
770 *Geophysical Research Letters*, **42**, doi:10.1002/2015GL063261

771 McFarquhar, M. G., and Roland List, 1991: The raindrop mean free path and collision rate  
772 dependence on rainrate for three-peak equilibrium and Marshall–Palmer distributions. *J.*  
773 *Atmos. Sci.*, **48**, 1999–2003.

774 Moncrieff, M. W., D. E. Waliser, M. J. Miller, M. A. Shapiro, G. R. Asrar, and J. Caughey,  
775 2012: Multiscale convective organization and the YOTC virtual global field campaign.  
776 *Bulletin of the American Meteorological Society*, **93**, 1171-1187.

777 Morton, B. R., G. I. Taylor, J. S. Turner, 1956: Turbulent gravitational convection for maintained  
778 and instantaneous sources, *Proc. Roy. Soc. London, A* **234**, 1-23.

779 Nakajima, T., and M. Tanaka, 1986: Matrix formulations for the transfer of solar radiation in a  
780 plane-parallel scattering atmosphere. *Journal of Quantitative Spectroscopy and Radiative*  
781 *Transfer*, **35**, 13-21.

782 Orville, R. E., and R. W. Henderson, 1986: Global Distribution of Midnight Lightning:  
783 September 1977 to August 1978. *Mon. Wea. Rev.*, **114**, 2640–2653. doi:  
784 [http://dx.doi.org/10.1175/1520-0493\(1986\)114<2640:GDOMLS>2.0.CO;2](http://dx.doi.org/10.1175/1520-0493(1986)114<2640:GDOMLS>2.0.CO;2)

785 Pielke, R. A., 2001: Influence of the spatial distribution of vegetation and soils on the prediction  
786 of cumulus convective rainfall. *Reviews of Geophysics*, **39**, 151-177.

787 Pielke, R. A., 2013: Mesoscale Meteorological Modeling, 3<sup>rd</sup> Edition, 760 pp., Academic Press,  
788 Waltham, Mass., ISBN:9780123852373.

789 Pulliainen, J., and M. Hallikainen, 2001: Retrieval of regional snow water equivalent from space-  
790 borne passive microwave observations. *Remote sensing of environment*, **75**, 76-85.

791 Robinson, F., S. Sherwood, D. Gerstle, C. Liu, and D. Kirshbaum, 2011: Exploring the land-  
792 ocean contrast in convective vigor using islands. *Journal of the Atmospheric Sciences*, **68**,  
793 602-618.

794 Roh, W., and Satoh, M., 2014: Evaluation of precipitating hydrometeor parameterizations in a  
795 single-moment bulk microphysics scheme for deep convective systems over the tropical  
796 open ocean. *J. Atmos. Sci.*, **71**, 2654-2673

797 Rosenfeld, D., and W. L. Woodley, 2000: Deep convective clouds with sustained supercooled  
798 liquid water down to -37.5 c. *Nature*, **405**, 440-442.

799 Rutledge, S. A., and P. V. Hobbs, 1983: The mesoscale and microscale structure and  
800 organization of clouds and precipitation in midlatitude cyclones. Viii: A model for the  
801 "seeder-feeder" process in warm-frontal rainbands. *J. Atmos. Sci.*, **40**, 1185-1206.

802 Saleeby M. S. and Susan C. van den Heever, 2013: Developments in the CSU-RAMS Aerosol  
803 Model: Emissions, Nucleation, Regeneration, Deposition, and Radiation. *J. Appl. Meteor.*  
804 *Climatol.*, **52**, 2601–2622. doi: <http://dx.doi.org/10.1175/JAMC-D-12-0312.1>

805 Satoh, M., T. Matsuno, H. Tomita, H. Miura, T. Nasuno, and S. Iga, 2008: Nonhydrostatic  
806 icosahedral atmospheric model (nicam) for global cloud resolving simulations. *Journal of*  
807 *Computational Physics*, **227**, 3486-3514.

808 Satoh, M., Tomita, H., Yashiro, H., Miura, H., Kodama, C., Seiki, T., Noda, A. T., Yamada, Y.,  
809 Goto, D., Sawada, M., Miyoshi, T., Niwa, Y., Hara, M., Ohno, Y., Iga, S., Arakawa, T.,  
810 Inoue, T., Kubokawa, H. (2014), The Non-hydrostatic Icosahedral Atmospheric Model:  
811 Description and development. *Progress in Earth and Planetary Science*. 1, 18.  
812 doi:10.1186/s40645-014-0018-1

813 Satoh, M., Inoue, T., and Miura, H., 2010: Evaluations of cloud properties of global and local  
814 cloud system resolving models using CALIPSO/CloudSat simulators. *J. Geophys. Res.*,  
815 115, D00H14, doi:10.1029/2009JD012247.

816 Schumacher, C., and R. A. Houze Jr. (2003), The TRMM precipitation radar's view of shallow,  
817 isolated rain, *J. Appl. Meteorol.*, 42, 1519– 1524.

818 Spencer, R. W., H. M. Goodman, and R. E. Hood, 1989: Precipitation Retrieval over Land and  
819 Ocean with the SSM/I: Identification and Characteristics of the Scattering Signal. *J. Atmos.*  
820 *Oceanic Technol.*, **6**, 254–273.

821 Stephens, G. L., N. B. Wood, and L. A. Pakula (2004), On the radiative effects of dust on  
822 tropical convection, *Geophys. Res. Lett.*, **31**, L23112, doi:10.1029/2004GL021342.

823 Stephens, G. L., and N. B. Wood, 2007: Properties of Tropical Convection Observed by  
 824 Millimeter-Wave Radar Systems. *Mon. Wea. Rev.*, **135**, 821–842. doi:  
 825 <http://dx.doi.org/10.1175/MWR3321.1>

826 Stull, R., 1988: *An Introduction to Boundary Layer Meteorology*. Kluwer Academic, 818 pp.

827 Takahashi, T., 1978. Riming electrification as a charge generation mechanism in thunderstorms.  
 828 *J. Atmos. Sci.* 35, 1536 – 1548.

829 Tao, W.-K. et al., 2003: Microphysics, radiation and surface processes in the goddard cumulus  
 830 ensemble (GCE) model. *Meteorol. Atmos. Phys.*, **82**, 97-137.

831 Tao, W.-K., W. Lau, J. Simpson, J.-D. Chern, R. Atlas, D. Randall, M. Khairoutdinov, J.-L. Li,  
 832 D. E. Waliser, and J. Jiang, 2009: A multiscale modeling system: Developments,  
 833 applications, and critical issues. *Bulletin of the American Meteorological Society*, **90**, 515-  
 834 534.

835 Tao, W.-K., X. Li, A. Khain, T. Matsui, and S. Lang, 2007: Role of atmospheric aerosol  
 836 concentration on deep convective precipitation: Cloud-resolving model simulations. *J.*  
 837 *Geophys. Res.*, **112**, doi:10.1029/2007JD008728.

838 Tao, W.-K., S. Lang, X. Zeng, X. Li, T. Matsui, K. Mohr, D. Posselt, J. Chern, C. Peters-Lidard,  
 839 and P. M. Norris, 2014: The goddard cumulus ensemble model (GCE): Improvements and  
 840 applications for studying precipitation processes. *Atmospheric Research*, **143**, 392-424.

841 Tao, W.-K., J.-P. Chen, Z. Li, C. Wang, and C. Zhang, 2012: Impact of aerosols on convective  
 842 clouds and precipitation. *Rev. Geophys.*, **50**, doi:10.1029/2011RG000369.

843 Tao, W.K., and T. Matsui, 2015: Cloud-System Resolving Modeling and Aerosols. In: Gerald R.  
 844 North (editor-in-chief), John Pyle and Fuqing Zhang (editors). *Encyclopedia of*

845        *Atmospheric Sciences*, 2nd edition, Vol 4, pp. 222–231. doi:10.1016/B978-0-12-382225-  
846        3.00511-9

847    Tao, W.-K., D. Wu, S. Lang, J. Chern, C. Peters-Lidard, A. Fridlind, and T. Matsui (2016),  
848        High-resolution WRF simulations of a deep convective-precipitation system during MC3E:  
849        Part I: Comparisons between Goddard microphysics schemes and observations, *Journal of*  
850        *Geophysics Research* (submitted)

851    Tomita, H. and M. Satoh, 2004: A new dynamical framework of nonhydrostatic global model  
852        using the icosahedral grid. *Fluid Dyn. Res.*, 34, 357–400, DOI:10.1016/j.fluiddyn.

853    Tomita, H., 2008: New microphysics with five and six categories with diagnostic generation of  
854        cloud ice, *J. Meteorol. Soc. Jpn.*, 86A, 121–142.

855    Varble, A., E. J. Zipser, A. M. Fridlind, P. Zhu, A. S. Ackerman, J.-P. Chaboureaud, S. Collis, J.  
856        Fan, A. Hill, and B. Shipway (2014), Evaluation of cloud-resolving and limited area model  
857        intercomparison simulations using TWP-ICE observations: 1. Deep convective updraft  
858        properties, *J. Geophys. Res. Atmos.*, 119, 13,891–13,918, doi:10.1002/2013JD021371.

859    Wall, C., C. Liu, and E. Zipser (2013), A climatology of tropical congestus using CloudSat, *J.*  
860        *Geophys. Res. Atmos.*, 118, 6478–6492, doi:10.1002/jgrd.50455.

861    Wallace, J. M. (1975), Diurnal variations in precipitation and thunderstorm frequency over the  
862        conterminous United States, *Mon. Weather Rev.*, 103, 406–419, doi:10.1175/1520-  
863        0493(1975)103<0406:DVIPAT>2.0.CO;2.

864    Wang, J.-J., R. F. Adler, G. J. Huffman, and D. Bolvin, 2014: An updated TRMM composite  
865        climatology of tropical rainfall and its validation. *Journal of Climate*, **27**, 273–284.

866    Weisman, M. L., W. C. Skamarock, and J. B. Klemp, 1997: The resolution dependence of  
867        explicitly modeled convective systems. *Monthly Weather Review*, **125**, 527–548.

868 Williams, E., and N. Renno, 1993: An Analysis of the Conditional Instability of the Tropical  
869 Atmosphere. *Mon. Wea. Rev.*, **121**, 21–36.

870 Williams, E. et al., 2002: Contrasting convective regimes over the Amazon: Implications for  
871 cloud electrification. *Journal of Geophysical Research*, **107**, D20, 8082-8101.

872 Williams, E., and S. Stanfill, 2002: The physical origin of the land–ocean contrast in lightning  
873 activity. *Comptes Rendus Physique*, **3**, 1277-1292.

874 Williams, E., T. Chan, and D. Boccippio (2004), Islands as miniature continents: Another look at  
875 the land-ocean lightning contrast, *J. Geophys. Res.*, 109, D16206,  
876 doi:10.1029/2003JD003833.

877 Williams, E., V. Mushtak, D. Rosenfeld, S. Goodman, and D. Boccippio, 2005: Thermodynamic  
878 conditions favorable to superlative thunderstorm updraft, mixed phase microphysics and  
879 lightning flash rate. *Atmospheric Research*, **76**, 288-306.

880 Yuter, S. E., and R. A. Houze Jr., 1995: Three-dimensional kinematic and microphysical  
881 evolution of Florida cumulonimbus. Part II: Frequency distributions of vertical velocity,  
882 reflectivity, and differential reflectivity. *Mon. Wea. Rev.*, 123, 1941–1963.

883 Zipser, E. J., C. Liu, D. J. Cecil, S. W. Nesbitt, and D. P. Yorty, 2006: Where are the most  
884 intense thunderstorms on earth? *Bulletin of the American Meteorological Society*, **87**, 1057-  
885 1071.

886 Zipser, E. J., 2003: Some Views On "Hot Towers" after 50 Years of Tropical Field Programs and  
887 Two Years of TRMM Data. *Meteorological Monographs* **29** (51): 49–58.



## List of Figures and Tables Captions

Table 1. Summary of model set up and physics options.

Figure 1. 14-year climatology of precipitating cloud classification via combined VIRS  $Tb_{IR}$  and PR  $H_{ET}$  criteria. a) Joint  $Tb_{IR}$  - $H_{ET}$  diagrams and normalized frequencies of different cloud-precipitation categories grouped over tropical ocean and tropical land (SW: *shallow warm*, SC: *shallow cold*, MW: *mid-warm*, MC: *mid-cold*, D: *deep*), and land-ocean difference. b) Spatial variability of normalized frequencies of cloud-precipitation categories on each  $2.5 \times 2^\circ$  grid boxes. Frequencies of five categories are summed up to 100% on each grid box.

Figure 2. a) 14-year climatology of contoured frequency with altitude diagrams (CFADs) of PR echo for each category grouped over tropical ocean and land (left) as well as land-ocean difference (right in the Tropics. b) 14-year climatology of the spatial variability of maximum (95% tile of probability are) echo and echo-top height for the *deep* category derived on each  $2.5 \times 2^\circ$  grid box. 95% tile of cumulative probability are used here to define “maximum” in order to remove statistical outliers.

Figure 3. a) 14-year climatology of cumulative probability distributions of  $PCTb_{85}$  (with a bin size of  $10^\circ\text{K}$ ) for each category grouped over ocean and land in the Tropics for each category (SW: *shallow warm*, SC: *shallow cold*, MW: *mid-warm*, MC: *mid-cold*, D: *deep*). b) 14-year

climatology of the spatial variability of the scattering index derived from the difference between the maxima and minima of  $PCTb_{85}$  derived on each  $2.5 \times 2^\circ$  grid box.

Figure 4. Diagram of continental convective invigoration theory from thermal and aerosol perspectives. Underlined text represents TRMM measurements in this manuscript. Over-ocean conditions are all in the opposite direction and not described here. Ultimate sources that characterize continental cloud and precipitation structures and microphysics as observed by the TRMM signals include the characteristics of the surface turbulent heat flux and aerosol concentrations.

Figure 5. a) 14-year times series of monthly PR CFAD composites of land-ocean difference at the midlevel of each class (SW: *shallow warm*, SC: *shallow cold*, MW: *mid-warm*, MC: *mid-cold*, D: *deep*). b) 14-year times series of monthly  $PCTb_{85}$  CPD composites of land-ocean difference for the *shallow warm*, *shallow cold*, *mid-warm*, *mid-cold*, and *deep* categories over tropical ocean.

Figure 6. a) Joint  $Tb_{IR} - H_{ET}$  precipitating cloud classification diagrams for June 2008 over the Tropics from TRMM observations, the MMF simulation, and the NICAM simulation over land and ocean (SW: *shallow warm*, SC: *shallow cold*, MW: *mid-warm*, MC: *mid-cold*, D: *deep*). b) Corresponding land-ocean differences in  $Tb_{IR} - H_{ET}$  diagrams.

Figure 7. a) CFADs of PR echoes for the *deep* category for June 2008 over the Tropics (except NICAM) from TRMM observations, the MMF simulation, and the NICAM simulation over land and ocean. b) Corresponding land-ocean CFAD differences.

Figure 8. a) Cumulative probability distributions of  $PCTb_{85}$  (with a bin size of  $10^\circ\text{K}$ ) for the *deep* category for June 2008 For more quantitative ways over the Tropics from TRMM observations, the MMF simulation, and the NICAM simulation over land and ocean. b) Corresponding land-ocean differences in cumulative  $PCTb_{85}$  distributions.

Figure 9. CFADs of vertical velocity over precipitation grids for both land and ocean from the MMF and NICAM simulations and their differences.

Figure 10. a) Frequencies of CAPE (in Joules per kg) and HLCL (in meters) over ocean and land derived from AIRS Level 2 retrievals, the MMF simulation, and the NICAM simulation for the large-scale environment. The MMF results are based on the GEOS grid; the NICAM CAPE and HLCL are derived from temperature and humidity fields averaged over a 40km footprint size, which is compatible with the AIRS Level 2 retrievals. b) Frequencies of lowest-layer relative humidity (RH) and surface evaporative fraction (EF) over ocean and land derived from the MMF and the NICAM simulations.

949

Name	NASA MMF	NICAM
Type	Hybrid Global Model with embedded 2D Cloud-Resolving Model (13,104 sets)	Global Cloud-Resolving Model (41,943,040 columns)
Horizontal Grid Spacing	2.5 x 2 deg (GEOS 4) 4 km (GCE)	3.5km in Average
Vertical Layers	44 layers up to stratosphere	40 layers up to stratosphere
Time Steps	1 hr (GEOS) 10 s (GCE)	15 sec
SST	NOAA weekly Optimum Interpolation SST analysis	NOAA weekly Optimum Interpolation SST analysis
LSM	CLM (Bonan et al. 2002)	bucket model (Kondo 1993)
Microphysics	Goddard 4ICE one-moment microphysics (Lang et al. 2014)	NICAM Single-moment Water 6 Tomita(NSW6) (Tomita 2008)

Table 1. Summary of model set up and physics options.

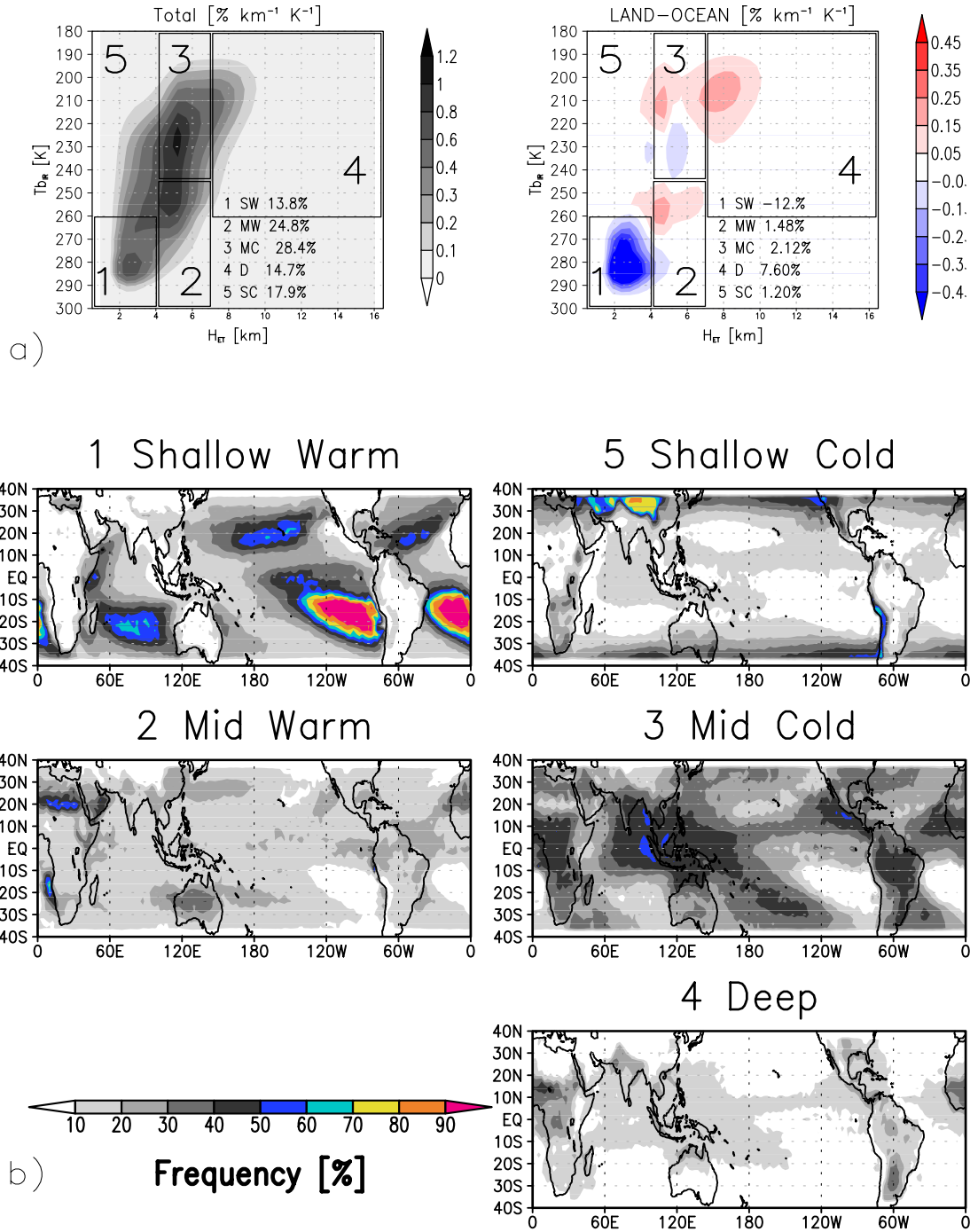


Figure 1. 14-year climatology of precipitating cloud classification via combined VIRS  $Tb_{IR}$  and PR  $H_{ET}$  criteria. a) Joint  $Tb_{IR}$  - $H_{ET}$  diagrams and normalized frequencies of different cloud-precipitation categories grouped over tropical ocean and tropical land (SW: *shallow warm*, SC: *shallow cold*, MW: *mid-warm*, MC: *mid-cold*, D: *deep*), and land-ocean difference. b) Spatial variability of normalized frequencies of cloud-precipitation categories on each  $2.5 \times 2^\circ$  grid boxes. Frequencies of five categories are summed up to 100% on each grid box.

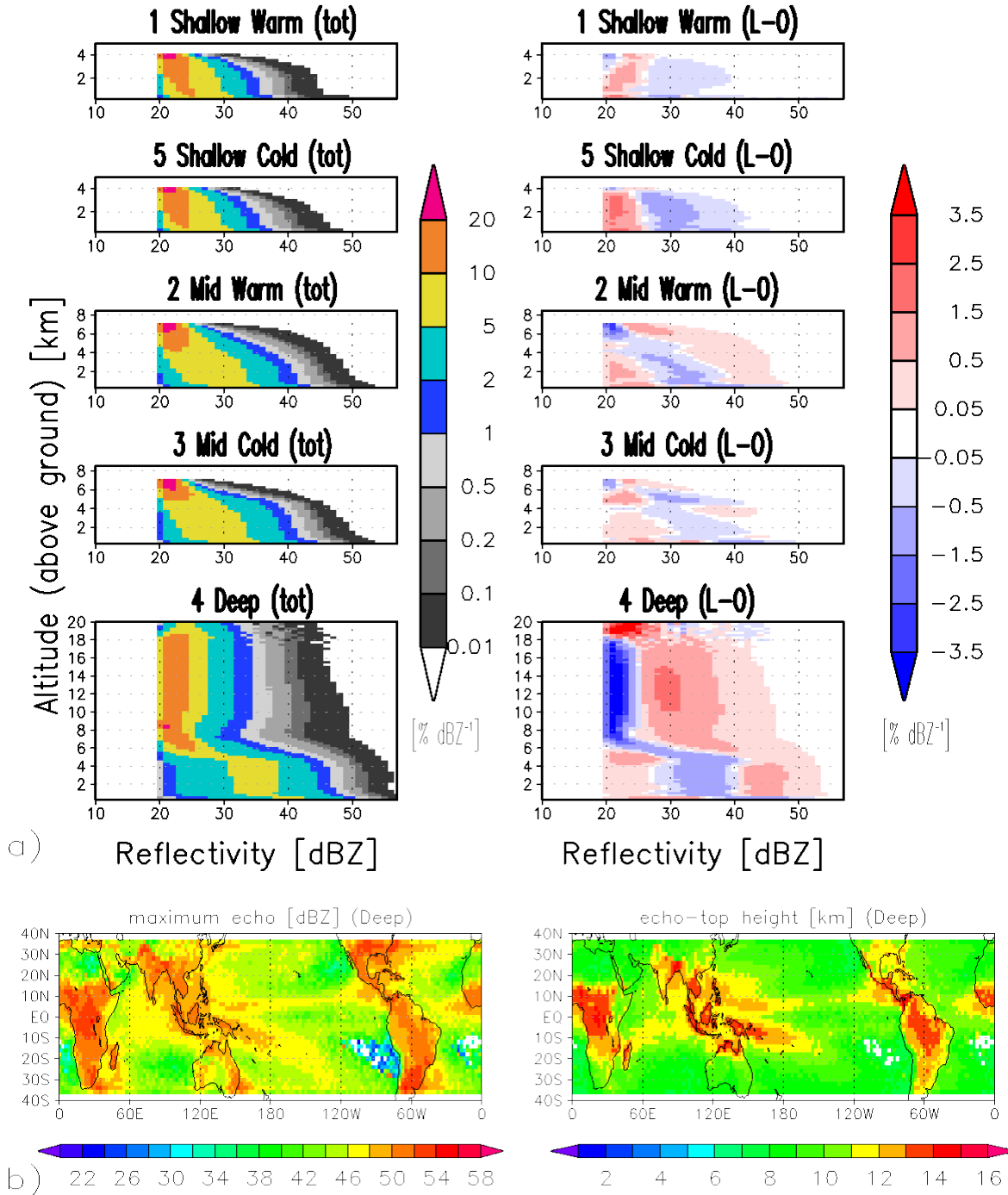


Figure 2. a) 14-year climatology of contoured frequency with altitude diagrams (CFADs) of PR echo for each category grouped over tropical ocean and land (left) as well as land-ocean difference (right in the Tropics). b) 14-year climatology of the spatial variability of maximum (95% tile of probability are) echo and echo-top height for the *deep* category derived on each 2.5 x 2° grid box. 95% tile of cumulative probability are used here to define “maximum” in order to remove statistical outliers.

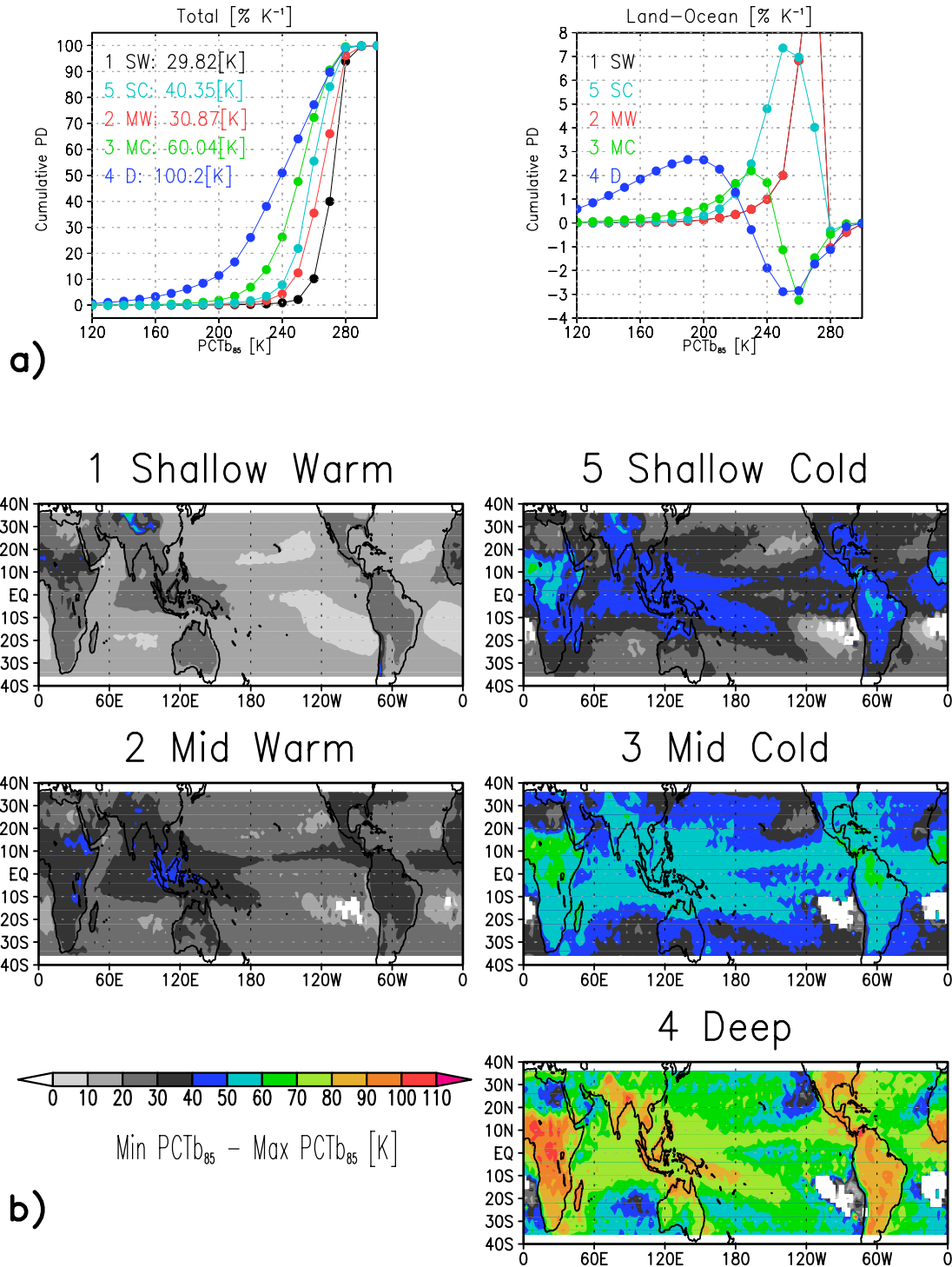
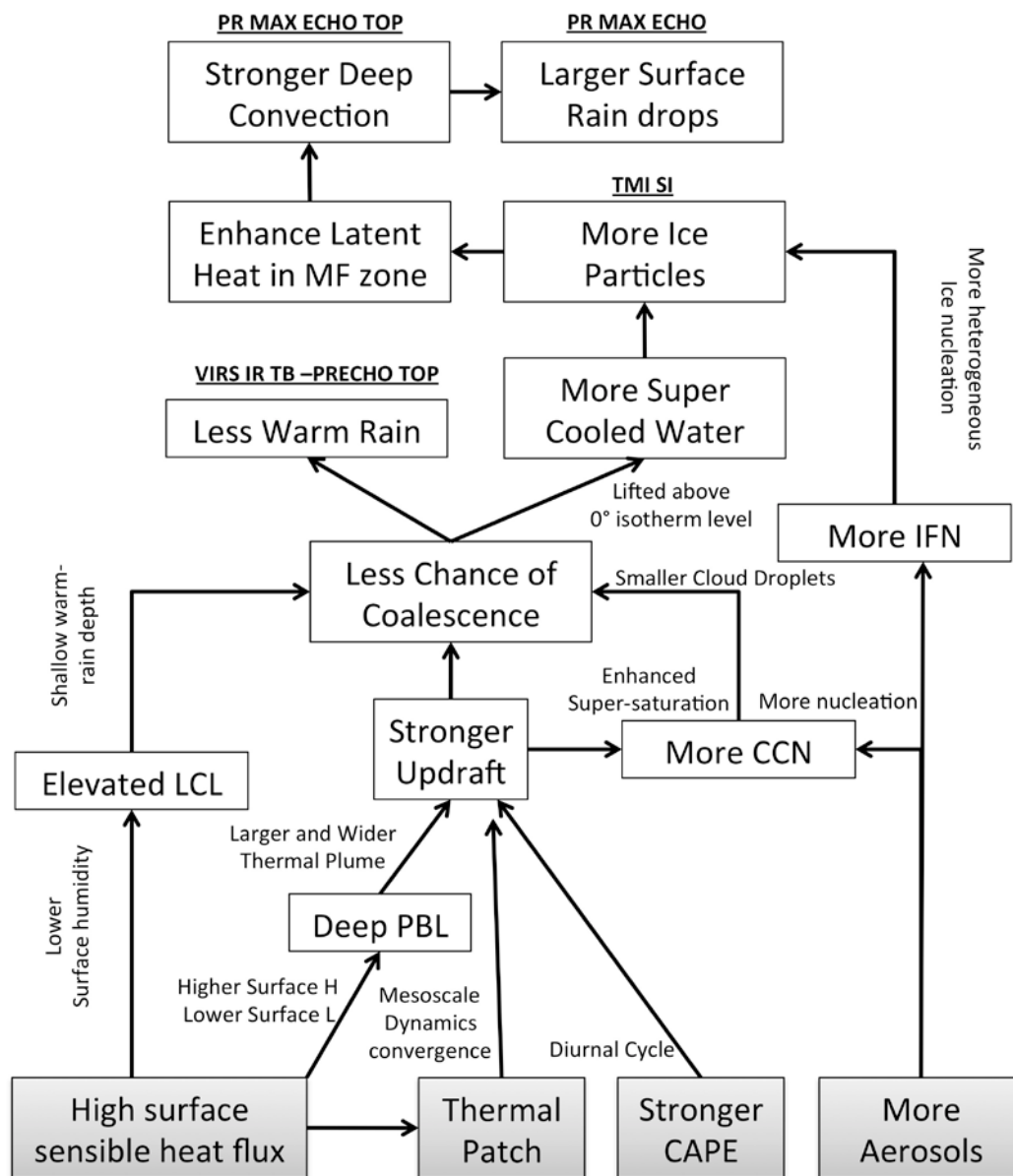


Figure 3. a) 14-year climatology of cumulative probability distributions of  $PCTb_{85}$  (with a bin size of  $10^{\circ}\text{K}$ ) for each category grouped over ocean and land in the Tropics for each category (SW: shallow warm, SC: shallow cold, MW: mid-warm, MC: mid-cold, D: deep). b) 14-year climatology of the spatial variability of the scattering index derived from the difference between the maxima and minima of  $PCTb_{85}$  derived on each  $2.5^{\circ} \times 2^{\circ}$  grid box.

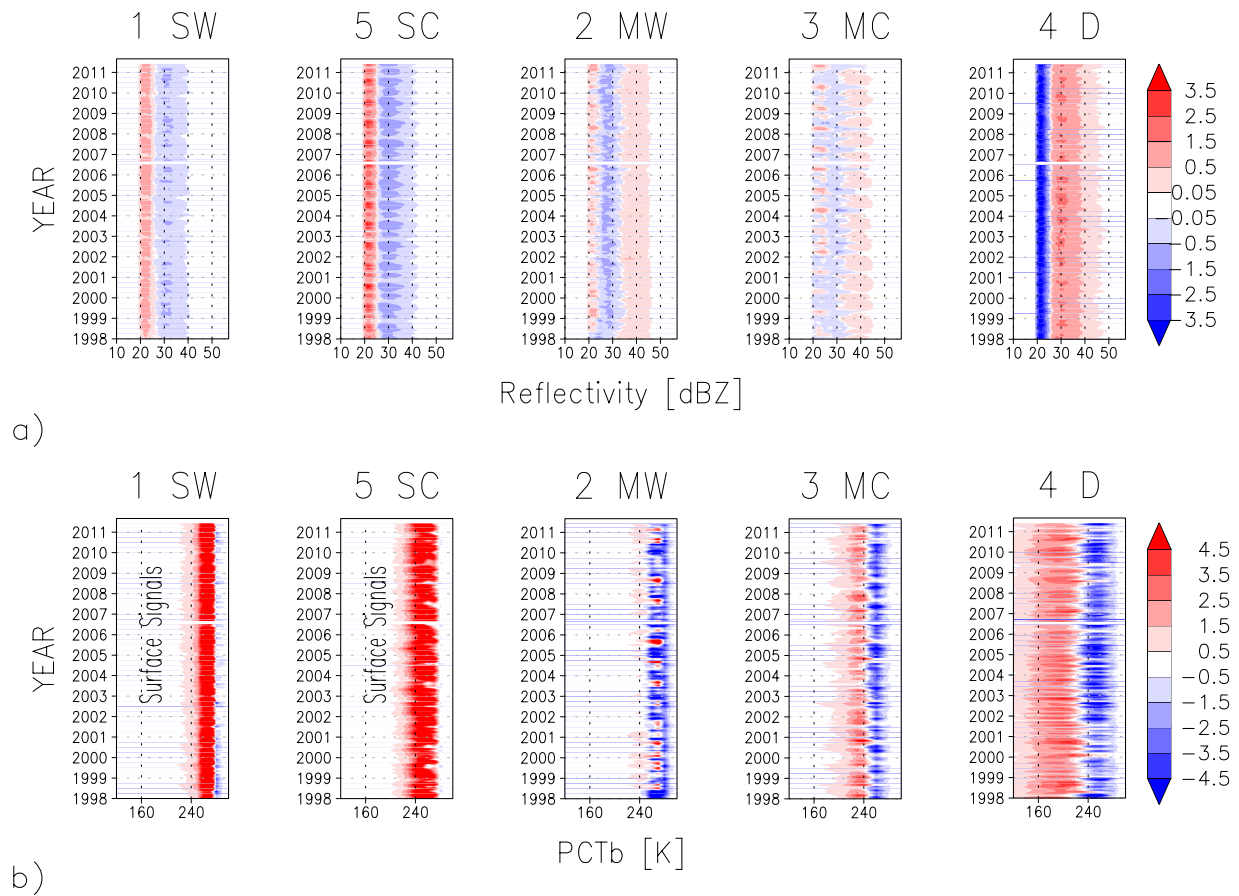


CONTINENTAL CONVECTION INVIGORATION DIAGRAM

Figure 4. Diagram of continental convective invigoration theory from thermal and aerosol perspectives. Underlined text represents TRMM measurements in this manuscript. Over-ocean conditions are all in the opposite direction and not described here. Ultimate sources that characterize continental cloud and precipitation structures and microphysics as observed by the TRMM signals include the characteristics of the surface turbulent heat flux and aerosol concentrations.



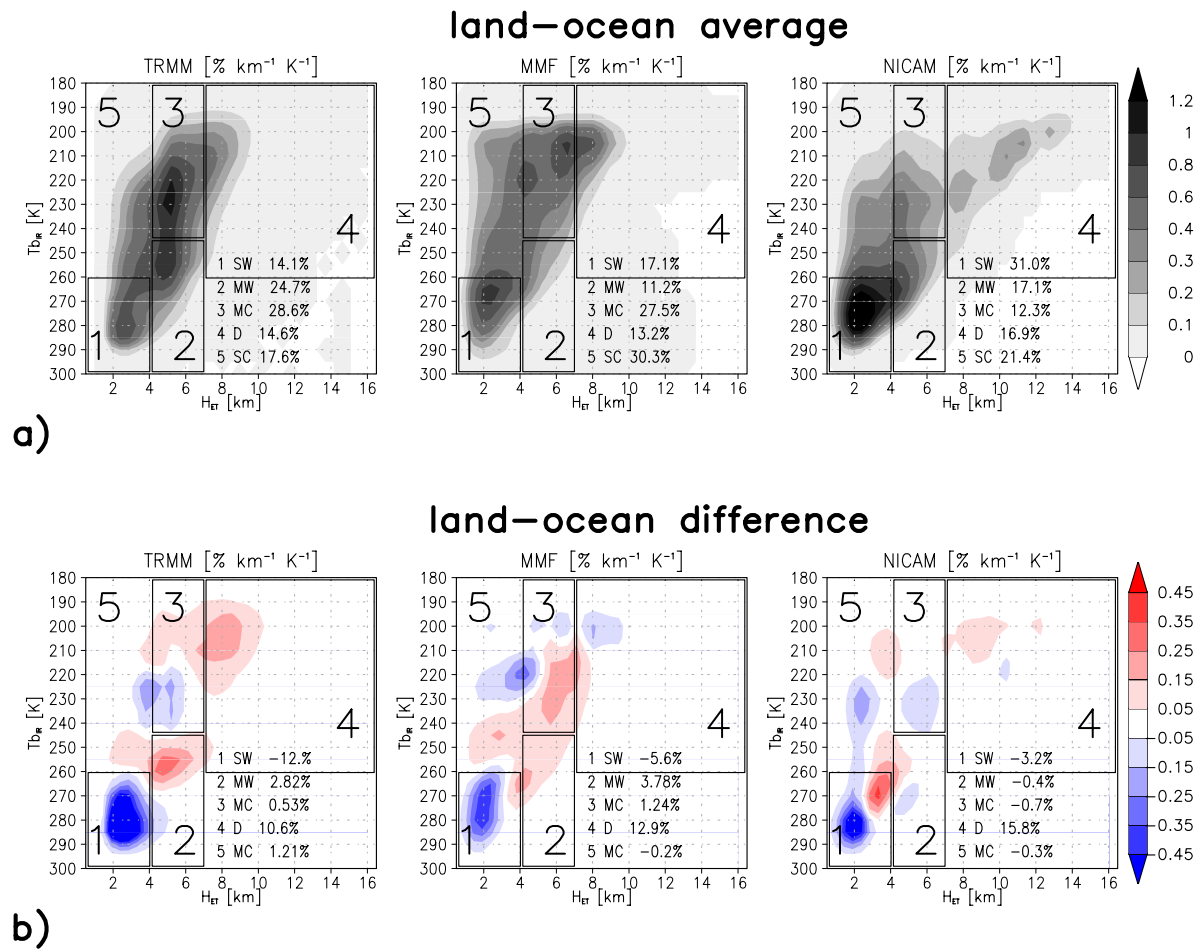
1005  
1006  
1007



1008  
1009  
1010  
1011  
1012  
1013  
1014  
1015  
1016  
1017  
1018  
1019  
1020  
1021  
1022  
1023  
1024  
1025  
1026  
1027

Figure 5. a) 14-year times series of monthly PR CFAD composites of land-ocean difference at the midlevel of each class (SW: *shallow warm*, SC: *shallow cold*, MW: *mid-warm*, MC: *mid-cold*, D: *deep*). b) 14-year times series of monthly  $PCTb_{85}$  CPD composites of land-ocean difference for the *shallow warm*, *shallow cold*, *mid-warm*, *mid-cold*, and *deep* categories over tropical ocean.

1028  
1029

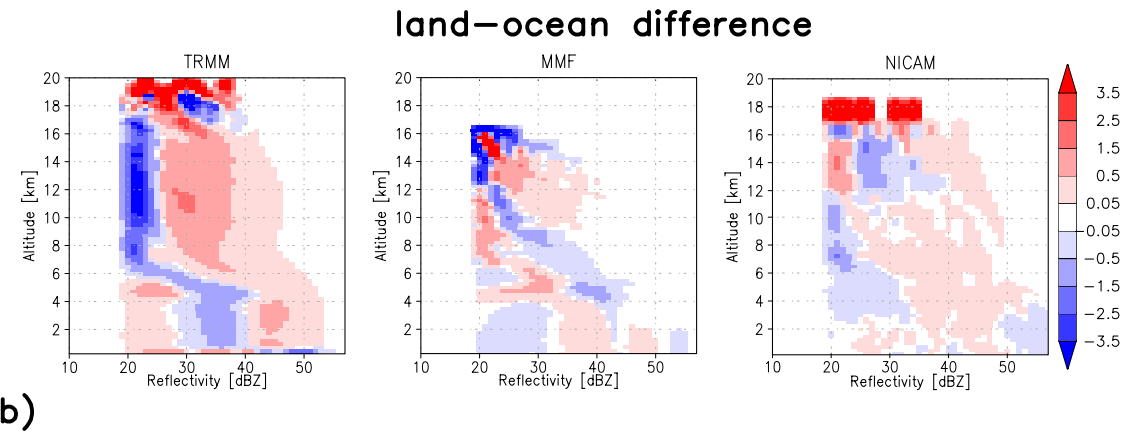
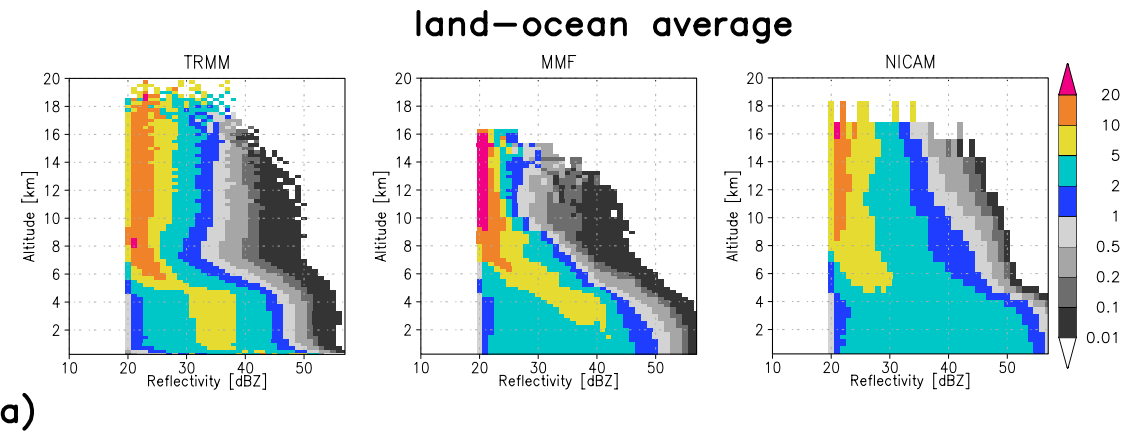


b)

1030  
1031  
1032  
1033  
1034  
1035  
1036  
1037  
1038  
1039  
1040  
1041  
1042  
1043  
1044  
1045  
1046

Figure 6. a) Joint  $Tb_{IR}$  -  $H_{ET}$  precipitating cloud classification diagrams for June 2008 over the Tropics from TRMM observations, the MMF simulation, and the NICAM simulation over land and ocean (SW: *shallow warm*, SC: *shallow cold*, MW: *mid-warm*, MC: *mid-cold*, D: *deep*). b) Corresponding land-ocean differences in  $Tb_{IR}$  -  $H_{ET}$  diagrams.

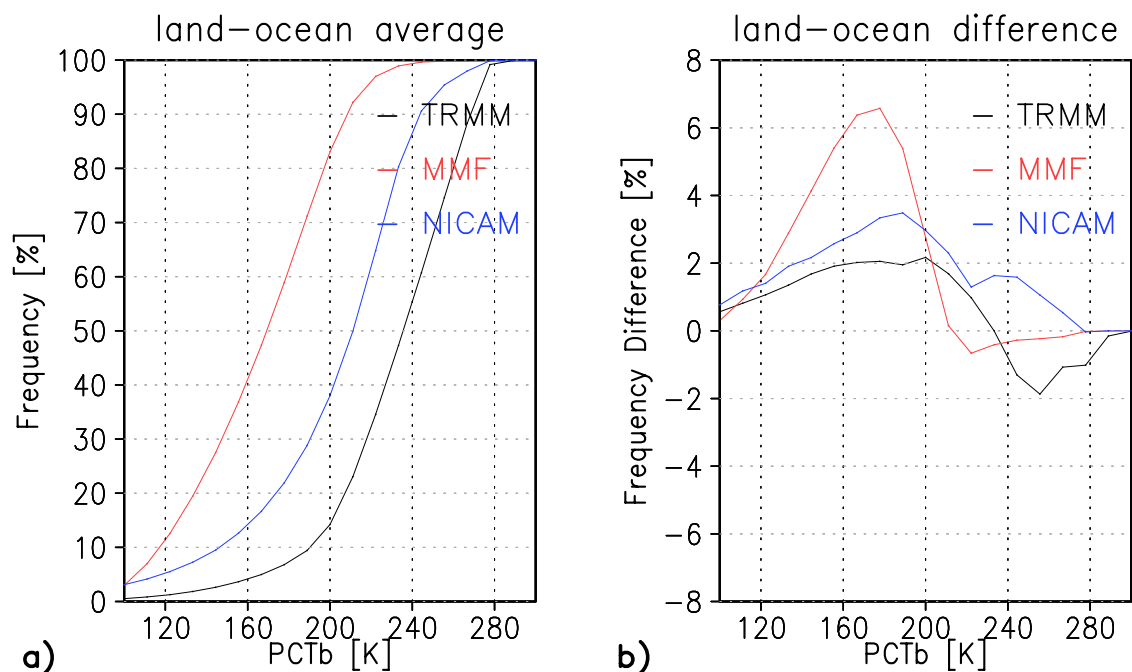
1047  
1048  
1049  
1050



1051  
1052  
1053  
1054  
1055  
1056  
1057  
1058  
1059  
1060  
1061  
1062  
1063  
1064  
1065  
1066  
1067  
1068

Figure 7. a) CFADs of PR echoes for the *deep* category for June 2008 over the Tropics (except NICAM) from TRMM observations, the MMF simulation, and the NICAM simulation over land and ocean. b) Corresponding land-ocean CFAD differences.

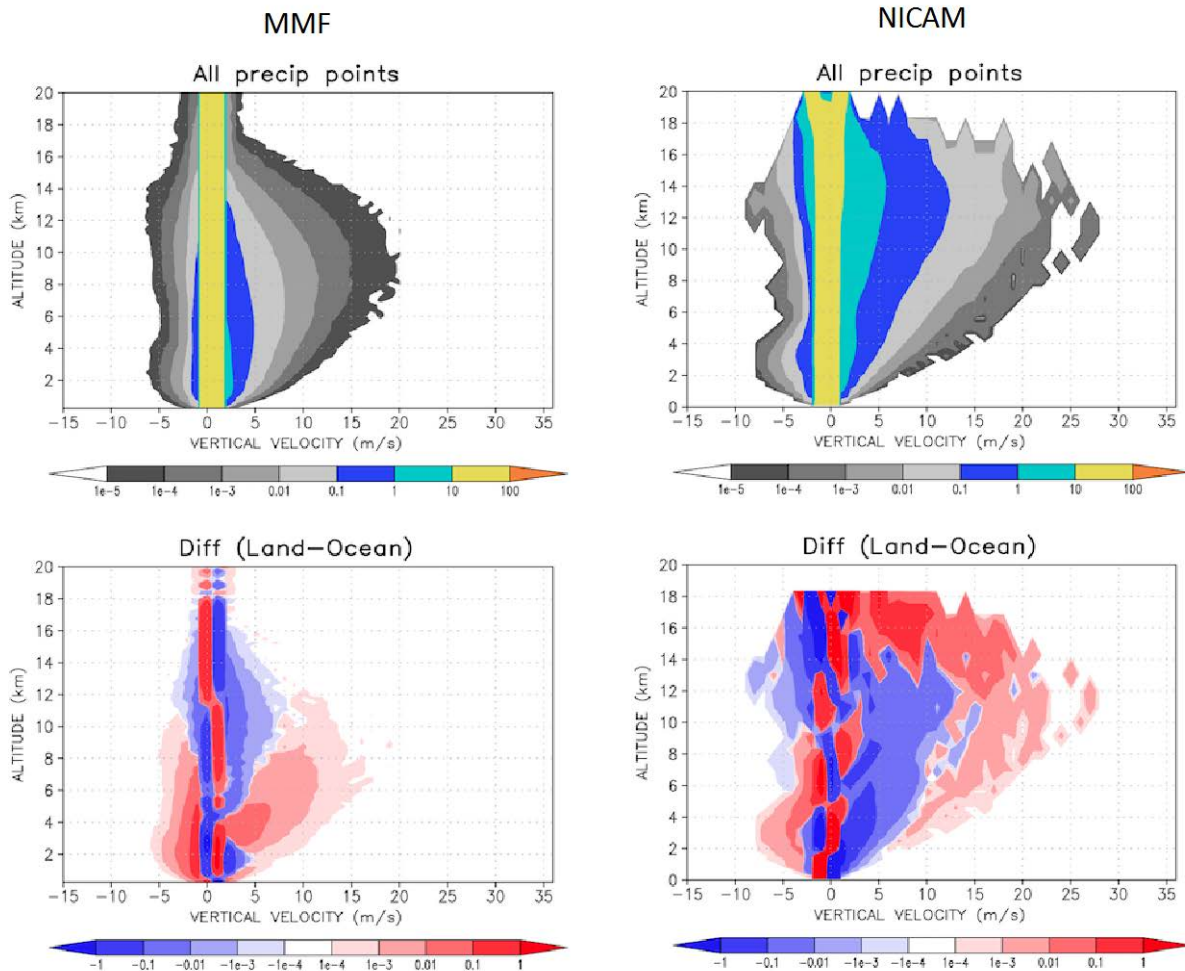
1069  
1070  
1071  
1072



1073  
1074  
1075  
1076  
1077  
1078  
1079  
1080  
1081  
1082  
1083  
1084  
1085  
1086  
1087  
1088  
1089  
1090  
1091  
1092  
1093  
1094  
1095  
1096

Figure 8. a) Cumulative probability distributions of  $PCTb_{85}$  (with a bin size of  $10^\circ\text{K}$ ) for the *deep* category for June 2008. For more quantitative ways over the Tropics from TRMM observations, the MMF simulation, and the NICAM simulation over land and ocean. b) Corresponding land-ocean differences in cumulative  $PCTb_{85}$  distributions.

1097  
1098  
1099  
1100

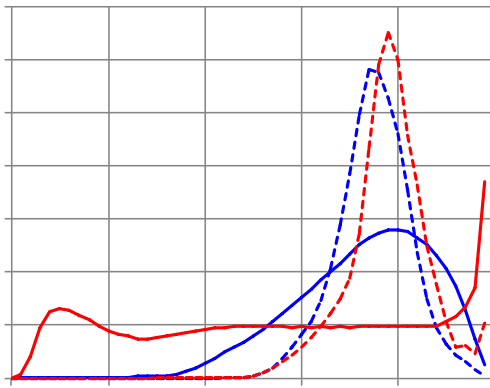


1101  
1102  
1103  
1104  
1105  
1106  
1107  
1108  
1109

Figure 9. CFADs of vertical velocity over precipitation grids for both land and ocean from the MMF and NICAM simulations and their differences.

) ---MMF (ocean)

a)



b)

1110  
1111

1112 Figure 10. a) Frequencies of CAPE (in Joules per kg) and HLCL (in meters) over ocean and  
1113 land derived from AIRS Level 2 retrievals, the MMF simulation, and the NICAM simulation for  
1114 the large-scale environment. The MMF results are based on the GEOS grid; the NICAM CAPE  
1115 and HLCL are derived from temperature and humidity fields averaged over a 40km footprint  
1116 size, which is compatible with the AIRS Level 2 retrievals. b) Frequencies of lowest-layer  
1117 relative humidity (RH) and surface evaporative fraction (EF) over ocean and land derived from  
1118 the MMF and the NICAM simulations.